Marine Chemistry 253 (2023) 104250

Contents lists available at ScienceDirect

Marine Chemistry

journal homepage: www.elsevier.com/locate/marchem

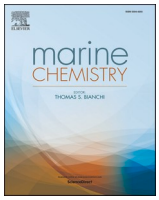

Volcanogenic fluxes of iron from the seafloor in the Amundsen Sea, West Antarctica

Lisa C. Herbert [a,*], Allison P. Lepp [b], Santiago Munevar Garcia [b], Arianne Browning [c], Lauren E. Miller [b], Julia Wellner [d], Silke Severmann [a], Claus-Dieter Hillenbrand [e], Joanne S. Johnson [e], Robert M. Sherrell [a,f]

[a] Department of Marine and Coastal Sciences, Rutgers University, 71 Dudley Rd., New Brunswick, NJ 08901, USA
[b] Department of Environmental Sciences, University of Virginia, 291 McCormick Rd., Charlottesville, Virginia 22903, USA
[c] Washington College, 300 Washington Ave, Chestertown, MD 21620, USA
[d] Department of Earth and Atmospheric Sciences, University of Houston, Science and Research Building 1, 3507 Cullen Blvd. #312, Houston, TX 77004, USA
[e] British Antarctic Survey, High Cross, Madingley Rd., Cambridge CB3 0ET, UK
[f] Department of Earth and Planetary Sciences, Rutgers University, 610 Taylor Rd., Piscataway, NJ 08854, USA

ARTICLE INFO

Keywords:
Thwaites Glacier
Marine sediment
Biogeochemistry
Antarctica
Iron flux
Trace metals
Volcanic glass
Polynya

ABSTRACT

The Amundsen Sea in the Pacific sector of West Antarctica receives meltwater from the fastest retreating Antarctic glaciers, and its coastal polynyas host the highest primary productivity per unit area observed on the Antarctic continental shelf. Polynya productivity provides the base for a robust, diverse ecosystem and is controlled primarily by light and the availability of the micronutrient iron (Fe). While the sources of Fe in the region are not yet certain, Fe could be transported within modified Circumpolar Deep Water (mCDW) that intrudes onto the retrograde shelf and into ice shelf cavities, where it gains buoyancy through the addition of glacial meltwater and is injected into the upper water column when it exits the cavity. Thus, fluxes of dissolved Fe from the seafloor into in-flowing mCDW may ultimately be a source of Fe to the euphotic zone in the Amundsen Sea. To investigate the surface sediment biogeochemistry and the potential for a significant benthic flux of Fe to the waters on the Amundsen Sea shelf, sediment cores were collected at two sites close to the calving fronts of the Pine Island and Thwaites Glacier ice shelves. Pore water was analyzed for trace element content, and sediment was analyzed for physical and chemical properties including organic carbon and trace elements. Using a novel approach based on hypothesized Fe speciation and colloidal particle radius, theoretical Fe fluxes were calculated from pore water gradients and porosity. The fluxes reveal a spatially variable Fe input to the lower water column that could ultimately fertilize primary productivity. Supported by geochemical and physical evidence, we conclude that submarine weathering of volcanic glass grains observed and quantified in seabed sediments at the Pine Island site drives nonreductive Fe fluxes that are 100-fold higher than at the Thwaites site. This study highlights the need for further investigations of benthic-pelagic coupling in the Amundsen Sea region, which will likely be impacted in coming decades by accelerating glacial melting.

1. Introduction

The Amundsen Sea drainage sector of the West Antarctic Ice Sheet (WAIS; Fig. 1) is undergoing rapid changes, with outlet glaciers such as Pine Island Glacier (PIG) and Thwaites Glacier (TG) at risk of melting and destabilization (Favier et al., 2014; Scambos et al., 2017; Holland et al., 2019). The primary concern in this region is the ongoing melting of ice-streams draining the WAIS and the resultant rise in global sea level (e.g., Hoffman et al., 2019; DeConto et al., 2021). However, the marine biogeochemical implications of glacier collapse have so far received less attention. Changes in ice-sheet dynamics with ongoing retreat are likely to impact the physical, chemical, and biological dynamics of polynyas in

Abbreviations: CDW, Circumpolar Deep Water; mCDW, modified Circumpolar Deep Water; WAIS, West Antarctic Ice Sheet; PIG, Pine Island Glacier; TG, Thwaites Glacier; MC, mega-corer; ICP-MS, inductively coupled plasma mass spectrometer; ICP-OES, inductively coupled plasma – optical emission spectrometry; SEM, scanning electron microscope; EDS, energy dispersive x-ray spectrometry.

* Corresponding author.
E-mail address: lherbert@marine.rutgers.edu (L.C. Herbert).

https://doi.org/10.1016/j.marchem.2023.104250
Received 10 February 2023; Received in revised form 31 May 2023; Accepted 1 June 2023
Available online 10 June 2023

the Amundsen Sea embayment, including the Amundsen Polynya adjacent to the Dotson and westernmost Getz ice shelves and the Pine Island Polynya in Pine Island Bay, adjacent to PIG (Fig. 1). Therefore, it is critical to understand the likely future impacts on the continental shelf ecosystem with continued WAIS melting.

On the Antarctic continental shelf, primary productivity is concentrated in coastal polynyas, which account for 65% of phytoplankton growth in shelf waters and host carbon fixation rates much higher (0.5–2.5 g C m^{-2} d^{-1}) than in the open Southern Ocean (0.2–0.4 g C m^{-2} d^{-1}) (Arrigo et al., 2008; Arrigo and van Dijken, 2003). The Amundsen Sea Polynya, for example, is the most productive of the Antarctic polynyas per area, supporting a diverse ecosystem (Arrigo et al., 2012). Productivity in the polynyas in this region is controlled by the availability of light and the micronutrient iron (Fe) (Alderkamp et al., 2015; Oliver et al., 2019). Forms of Fe available for biological uptake ("bioavailable Fe") may be delivered to the polynya via outflows from the cavities of the ice shelves that fringe the Amundsen Sea embayment (Sherrell et al., 2015; St-Laurent et al., 2019), and recent circum-Antarctic modeling suggests that this mechanism applies throughout the Antarctic margin (Dinniman and St-Laurent, 2020).

Warm Circumpolar Deep Water (CDW) initially invades the continental shelf at depth, mixes with Winter Water that lies above it to form modified CDW (mCDW), and then enters the ice shelf cavities to drive glacial melting primarily near the grounding line. Upon mixing with meltwater within the cavity, this water mass gains buoyancy and flows toward the ice shelf terminus and into the open coastal ocean at the depth of the ice shelf draft (Randall-Goodwin et al., 2015). This phenomenon is called the "meltwater pump," and is driven by the rate at which warm mCDW drives melting of the basal ice shelf (Greisman, 1979; Jenkins et al., 2016). Because mCDW interacts with shelf sediments *en route* to the ice shelf cavities, the meltwater pump may play an important role in advective coupling between the seafloor sediments and the euphotic zone.

The outflowing water mass formed by the meltwater pump is rich in Fe (e.g., 0.7 nM dissolved Fe and 90 nM particulate Fe for the Dotson Ice Shelf outflow; Sherrell et al., 2015; unpublished data) and is thought to be critical in sustaining intense polynya productivity throughout the growing season (Alderkamp et al., 2015; Sherrell et al., 2015; St-Laurent et al., 2019). Yet, the primary sources of Fe enrichment in this water mass are not well known. Based on recent observational and modeling studies, the Fe pool in the sub-surface outflow is likely a combination of 1) dissolved and particulate Fe released during basal ice-shelf melt or from glacial sediments proximal to the grounding zone (with a possible contribution from drainage of the subglacial hydrologic system, e.g. Malczyk et al., 2020), and 2) inflowing mCDW that has already incorporated additional dissolved Fe released from continental shelf sediments, as suggested by water column dissolved Fe measurements (Oliver et al., 2019; Sherrell et al., 2015; St-Laurent et al., 2019, 2017; van Manen et al., 2022). Iron supplied to the polynya by the outflow from the ice shelves is dominated by suspended particulate Fe, with a relatively high fraction of labile Fe and Mn oxide phases that may result from diagenesis or subglacial/submarine weathering of sediments upstream and downstream of the grounding line (Planquette et al., 2013; van Manen et al., 2022). However, water column Fe measurements suggest that, in the region of the Dotson Ice Shelf and the adjacent Amundsen Sea Polynya, mCDW flowing into the cavity has already acquired additional dissolved Fe equivalent to the concentrations observed in the outflow (Sherrell et al., 2015; van Manen et al., 2022). This suggests that benthic sediments likely add dissolved Fe to the mCDW before it mixes with glacial meltwater. Numerous studies have indicated the importance of a benthic Fe source to other Antarctic shelf regions as well, such as the Ross Sea and the western Antarctic Peninsula shelf (Hatta et al., 2017, 2013; Sherrell et al., 2018), and the Southern Ocean as a whole (Burdige and Christensen, 2022; Dinniman and St-Laurent, 2020; Sieber et al., 2021; Tagliabue et al., 2009).

Dissolved Fe^{2+} and Mn^{2+} can be released to the sediment pore water during early diagenesis following metabolic reduction of metal oxides by benthic microbes oxidizing sedimentary organic matter through

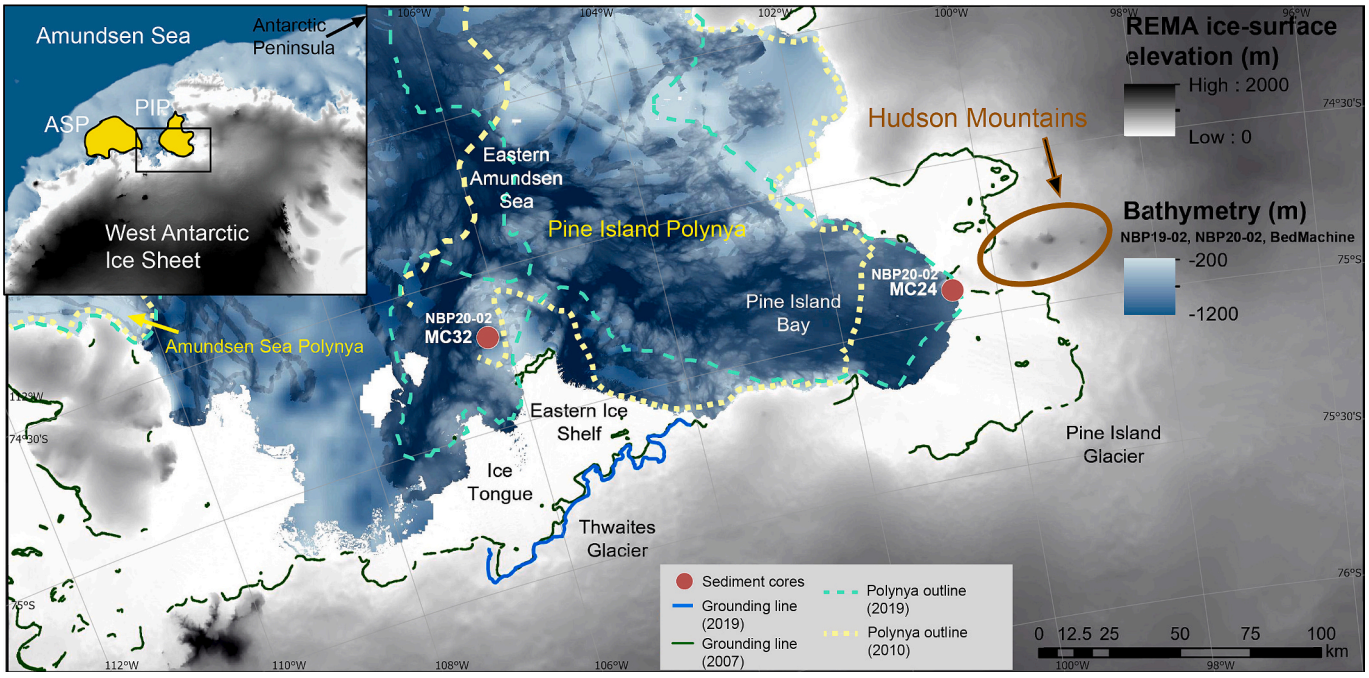

Fig. 1. Map of the study site adjacent to Pine Island and Thwaites Glaciers in the Amundsen Sea embayment. Red circles indicate the two sample sites: MC24/Pine Island (PIG) and MC32/Thwaites (TG). The polynya outlines (dashed lines) were derived from satellite images (MODIS/NSIDC) from December 2010 (yellow, short dashes) and February 2019 (green, longer dashes). Polygons showing the typical January positions of the Amundsen Sea Polynya (ASP) and Pine Island Polynya (PIP) are shown in yellow in the inset map. Multibeam data are from Hogan et al., 2020, collected during NBP19–02 and NBP20–02. The grounding lines are inSAR and are from Milillo et al., 2019 and Rignot et al., 2011. (For interpretation of the references to color in this figure legend, the reader is referred to the web version of this article.)

dissimilatory iron reduction (Lovley, 1993). This occurs in sediments once oxygen and nitrate have been depleted to concentrations that cannot support microbial metabolism, a state which is referred to as "suboxic" in this paper. The reduced, aqueous metals diffuse along pore water concentration gradients and can 1) precipitate as sulfide, carbonate, or oxide minerals depending on sediment geochemistry, or 2) cross the sediment-water interface through molecular diffusion, irrigation by benthic macrofauna, or sediment resuspension (Burdige, 1993; Canfield, 1989; Homoky et al., 2016). The reductive release of dissolved Fe from suboxic sediments is a well-established phenomenon (Berelson et al., 2003; Dale et al., 2015; Elrod et al., 2004; Homoky et al., 2012; Klar et al., 2017; Noffke et al., 2012; Severmann et al., 2010). However, previous biogeochemical studies of seafloor surface sediments near the Amundsen Sea Polynya indicated that despite high productivity, carbon oxidation rates are low in the consolidated sediments and oxygenation of the upper sediments is high compared to similar high-latitude systems (Choi et al., 2016; Kim et al., 2016). Therefore, nonreductive release of Fe from submarine mineral weathering must be considered in this setting. Nonreductive Fe release has been identified in oxygenated sediments, particularly those containing trace metal-rich, highly weatherable volcanic material (Homoky et al., 2021, 2013, 2011a; Longman et al., 2022). The Amundsen Sea embayment is adjacent to regions with evidence of past volcanism, including activity within the last 10,000 years (Rowley et al., 1990; Corr and Vaughan, 2008; Wilch et al., 1999), making a volcanic contribution to the offshore sediments feasible.

In this study we consider both reductive and nonreductive release mechanisms and their relative importance in Amundsen Sea sediments. To do so, we employ a novel method of quantifying nonreductive Fe flux to the overlying water based on high sensitivity mass spectrometric measurements of dissolved metals in porewater, and the possible size distribution of the expected organic Fe complexes and colloids that are included within the operationally defined "dissolved" fraction. Through geochemical analysis of two sediment cores located immediately offshore of Thwaites and Pine Island glaciers, we aim to determine variables controlling fluxes of benthic Fe that may be important in supporting the observed productivity in the Amundsen Sea Polynya. We find that benthic flux differs greatly between the two investigated sites, and that flux linked to nonreductive weathering of volcanic glass particles could be an important source of Fe to the water column. More broadly, our findings support previous studies arguing that early diagenesis of volcanogenic sediments could be an important source of trace metals to the water column in the global ocean (Homoky et al., 2011b; Longman et al., 2022).

2. Methods

2.1. Field sampling

We make use of two mega-corer (MC) subcores that were collected on research cruise *NBP20–02* aboard the *RV/IB Nathaniel B. Palmer*, the second of three expeditions under the Thwaites Offshore Research (THOR) initiative of the International Thwaites Glacier Collaboration (ITGC). Subcore MC24 (the PIG site; water depth 460 m; 74.9016° S, 100.5979° W) was recovered at the NE corner of the Pine Island Glacier Ice Shelf front, where CDW inflow under the Pine Island Ice Shelf dominates (e.g., Yoon et al., 2022), and subcore MC32 (the TG site; water depth 1043 m; 74.7014° S 106.2709° W) was collected north of the Thwaites Eastern Ice Shelf, near a location where also CDW inflow is recorded (Wåhlin et al., 2021; Fig. 1). The PIG site was located under the Pine Island Glacier Ice Shelf from at least 1947C.E., and probably since 10 ka (Arndt et al., 2018), until just 12 days before its recovery, when a major calving event took place (Yoon et al., 2022). Both coring sites were selected based on shipboard multibeam swath bathymetry to target undisturbed sediment (e.g., no seafloor evidence of iceberg ploughing).

All pore water and overlying water samples were conducted using all-plastic syringes and acid-cleaned Rhizons, model CSS, 8 cm length with mean pore size 0.15 μm (Dickens et al., 2007; Seeberg-Elverfeldt et al., 2005). Rhizons were inserted though pre-drilled holes in the core liner to sample interstitial pore water and overlying water (2 cm above the sediment-seawater interface). From each sampling interval, the first 1.0 mL of filtered water was discarded to sample-rinse the Rhizon before a sample volume of 2.0 mL was collected. Pore water samples were immediately acidified to 0.024 M ultrapure hydrochloric acid (HCl; 0.2% *v/v)* within the syringe, and a new Rhizon and syringe were used for each sampling interval. Acidified pore water was stored in acid-cleaned LDPE Nalgene bottles. Sediment samples were collected from parallel cores from the same MC deployment (<1 m distant from the pore water subcore) retrieved during the MC24 and MC32 deployments. Sediment samples were homogenized and stored in centrifuge tubes with no headspace for porosity analysis. All sampling tools were acid cleaned and rinsed with ultrapure water at the Department of Marine and Coastal Sciences at Rutgers University before the cruise. Pore water and sediment samples were stored and shipped at 4 °C.

2.2. Pore water analyses

Acidified pore water and overlying water samples were analyzed for dissolved aluminum (Al), barium (Ba), cadmium (Cd), cobalt (Co), chromium (Cr), Fe, Mn, molybdenum (Mo), nickel (Ni), phosphorus (P), titanium (Ti), uranium (U), vanadium (V), and yttrium (Y) using a Thermo Scientific Element 2 inductively coupled plasma mass spectrometer (ICP-MS) at Rutgers University. The full trace metal suite was analyzed to provide evidence for biogeochemical processes in the sediment that could be influencing Fe release. The multi-element standards were prepared in-house and matrix-matched with overlying seawater (assuming similar major ion composition as the pore water). Samples were diluted 20-fold before analysis, and drift and matrix corrections were based on In added to each solution. Determined blanks were <20% of lowest pore water samples for all elements except Cd and Cr, where blanks were 21–30%, and Mn, Co, and Ni where the lowest samples were in the same range as the blank. Precision, estimated by preparing and analyzing a sample in triplicate and calculating the percent relative standard deviation, was <±5% for all elements except Cd, Al, Ti, and Ni, which were <±15%.

Silicic acid was determined in 10-fold diluted pore waters and overlying waters by inductively coupled plasma – optical emission spectrometry (ICP-OES; Thermo iCAP 7000 series) against matrix-matched (Equatorial Pacific surface water) standards made from a NIST-traced single element silicon (Si) standard (High Purity Standards), using Y as a drift and matrix normalizer in all solutions. A working stock standard (3000 μM) for seawater Si analysis was obtained from the Ocean Data Facility at Scripps Institution of Oceanography (Susan Becker, pers. comm.) and run as an unknown to test accuracy and inter-laboratory agreement; results agreed within 7%. Blanks were <10% of determined values for all samples.

2.3. Solid phase analyses

For porosity determination, subsamples of solid sediment were weighed in vials of known mass and volume, then placed open in an oven at 60 °C and re-weighed once dry. The porosity (*v*/v) was calculated based on the known volume of sediment and the calculated volume of water (corrected for salt assuming 35 g/kg salt) lost on drying.

For organic carbon analysis, the dried sediments from the porosity analysis were powdered and weighed (~15–25 mg) into silver weigh boats, then acid fumed in a sealed container with an open beaker of concentrated hydrochloric acid for 24 h to remove carbonates. Total carbon contents (assumed to represent total organic carbon after carbonate removal) were analyzed on a CE Elantech Flash 2000 CHN analyzer (column configured for CNS analysis) at the New Jersey City University Geosciences Laboratory.

Laser diffraction particle size analysis was carried out using a Bettersizer S3 Plus with a green laser optimized for fine-grained sediments. Samples were treated with sodium hexametaphosphate to deflocculate the sediment grains in deionized water for at least 48 h prior to analysis. A magnetic stir bar was used to create a homogenized slurry from which aliquots were pipetted into the Bettersizer reservoir. Smear slides were made from each grain size sample and imaged using a Zeiss Axiolab 5 under plane-polarized light.

To quantify volcanic glass content in the Pine Island sediments, deflocculated sediment samples were sieved at 63 μm, 125 μm, 212 μm, and 300 μm and each fraction was dried and weighed. Each fraction was spread evenly across a microscope plate with a grid of 0.5 × 0.5 cm cells for counting. Between 300 and 500 grains in each fraction were counted under a Leica dissecting microscope and classified by appearance as "Pristine glass", "Other volcanics" or "Not volcanic." "Pristine glass" grains were not visibly weathered and were characterized as exhibiting: 1) vesicles and/or conchoidal fracturing, 2) brown coloration, 3) translucency, and 4) a glassy luster in reflected light. "Other volcanics" were identified as having visible vesicles, but only some, not all, of the other characteristics of pristine glass listed above. This second category likely includes originally pristine glass particles that had been subsequently weathered, physically altered by erosion and transport, and/or were coated by other minerals. The "Not volcanic" fraction consisted of a variety of other minerals including quartz and micas, as well as occasional foraminifera tests. The mass of each class was converted to estimated volume based on the ratio of volcanics to other minerals using grain densities of 2.3 g cm^{-3} for the volcanic glass and 2.7 g cm^{-3} for the other minerals (Shipley and Sarna-Wojcicki, 1982). The volume fraction of glass in each sediment sample was estimated based on porosity.

Sieved samples (>63 μm fraction) were examined under a stereoscope and approximately 30 volcanic grains were mounted and sputter coated (gold-palladium) for imaging with an FEI Quanta 650 field-emission gun scanning electron microscope (SEM) in high-vacuum mode. After imaging was completed, characteristic x-rays were measured using energy dispersive x-ray spectrometry (EDS) and translated into energy spectra and elemental abundance using AZtec software. The EDS spectra were collected at 15.00 kV, spot size of 5.0 μm, and a working distance of 10.0 mm. Elements of interest, including Si, Al, magnesium (Mg), Ti, and Fe were included. Several outlier spectra had substantially different elemental compositions than the rest (even on the same grain), presumably due to incomplete cleaning of the grain surface or the formation of secondary minerals on the glass surface and were not included in compositional averages. Four spectra exhibited high Mg and low Al contents and may have represented Mg (hydr)oxides, while two other spectra exhibited high calcium (Ca) and Fe, possibly representing a mixed Fe and Ca sulfate or carbonate precipitate. The remaining 14 spectra were from 8 unique grains from 5 sample depths, with a relative standard deviation of <20% for Ca, Ti, and Fe, <11% for Al and Si, and <5% for oxygen (O), sodium (Na), and Mg.

Extractions of reactive Fe and Mn phases were conducted following a modification of the sequential extraction in Poulton and Canfield (2005). Wet sediments were mixed with 1 M hydroxylamine HCl in 25% *v/v* (4.35 M) acetic acid and agitated continuously for 48 h at room temperature. The samples were then centrifuged, the supernatant removed for analysis, and the process was repeated with 50 g/L (0.29 M) dithionite buffered with sodium citrate with continuous agitation for 2 h at room temperature. The concentrations of Fe and Mn in both extracts were analyzed using ICP-OES on an iCAP 7500 instrument at Rutgers University. Standards and blanks were matrix matched with the corresponding extract solution (hydroxylamine HCl or dithionite). Instrument drift was monitored using yttrium additions and no drift was observed. Two procedural blanks were similar to instrumental blanks, indicating no contamination occurred during sample processing.

To determine total elemental composition, dried homogenized sediments were subsampled (50 mg) and digested in Teflon PFA screw-cap vials (Savillex), using a mixture of concentrated HNO_3 and HF. Digests were then dried on a hotplate in a clean HEPA hood and taken up again in 6 M HCl until fully dissolved. For analysis by quadrupole ICP-MS (Thermo iCAP Q operated in KEDS mode), samples were dried down again and re-dissolved in 2% (*v/v*) HNO_3. Concentrations were determined using mixed element standards and several certified reference materials were digested and analyzed in the same session (marine sediment MAG-1, basalt BCR-1, and estuarine mud 1646), with indium used as a matrix normalizer and drift monitor for all samples, standards, and blanks. Blanks were <0.1% of lowest signal for all reported elements. Determined values for the reference materials agreed with certified values, within certified uncertainty.

2.4. Flux determination

Benthic fluxes of Fe across the sediment-water interface at both sites were calculated assuming molecular diffusion only using a model based on Fick's first law (Boudreau, 1997):

$$J = \varphi D_{sed} \frac{dC}{dz} \quad (1)$$

where J = the flux of Fe, φ = porosity of the sediment, D_{sed} = the effective diffusion coefficient for Fe, and dC/dz = partial differential of concentration with respect to vertical distance into the sediment, for the uppermost infinitely small interval in depth, approximated here as the gradient between the uppermost sample, 0.5 cm below sea floor (cmbsf), and the overlying water. Note that the overlying water values used for this calculation were likely influenced by disturbance during sampling or contamination from coring equipment, making the estimated gradients lower than they would be in situ. Positive values of J indicate a flux from the sediment to the water column.

Values of D_{sw} for non-ionic Fe phases were determined from the Stokes-Einstein relation:

$$D_{sw} = \frac{kT}{6\pi\eta r_s} \quad (2)$$

where k = the Boltzmann constant (1.38×10^{-23} J K^{-1}), T = the temperature (K), η = the viscosity of the solvent (kg m^{-1} s^{-1}), and r_s = the hydrodynamic radius of the ligand or colloid (nm). Diameters were selected to represent realistic values for organic ligands such as siderophores (1 nm; Baars et al., 2014; Vraspir and Butler, 2009), fresh ferrihydrite nanoparticles (30 nm; Wells et al., 1991), the purported predominant colloid size in seawater (65 nm; Vaillancourt and Balch, 2000), and an average value used previously for Fe colloids in the Southern Ocean (150 nm; Boye et al., 2010). Salinity and temperature values representing mCDW in the vicinity of the core locations were taken from the literature. All variables used in the flux determination are given in Supplementary Table 1.

3. Results

3.1. Pore water trace metal concentrations

Concentrations of dissolved Fe in the pore water at the PIG site were low (<1000 nM), with the exception of two peaks of 5100 nM and 2800 nM at 0.5 cmbsf and 2.5 cmbsf, respectively (Fig. 2A). At the Thwaites Glacier (TG) site, Fe concentrations remained very low (<100 nM) down to 5 cmbsf, then rose to a peak of 8500 nM at 8 cmbsf (Fig. 2A). At Pine Island, the pore water Fe concentrations correlated (Pearson correlation coefficient $r > 0.8$) with Al, Co, Mn, Y, and Ti, while at TG, pore water Fe correlated less strongly (r between 0.62 and 0.82) with Co, Mn, Ni, Y, Pb, and Cd (Table 1; Supplemental Fig. 1).

Pore water Al and Ti profiles are similar in shape to that of Fe at the PIG site, with elevated concentrations at 0.5 and 2.5 cmbsf of 4400–7200 nM for Al and 300–500 nM for Ti (Fig. 2B, C). At the TG site, pore water concentrations of Al and Ti are much lower (<900 nM Al and

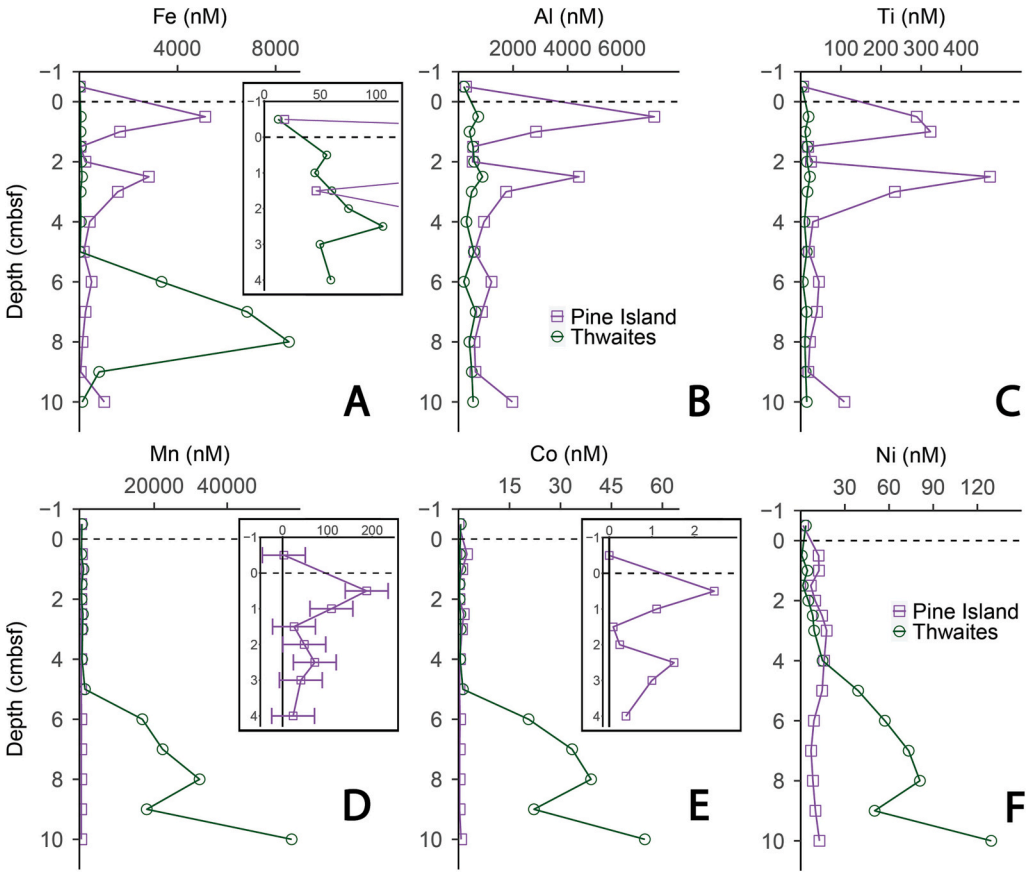

Fig. 2. Profiles of pore water Fe (A), Al (B), Ti (C), Mn (D), Co (E), and Ni (F) concentrations vs. depth in the sediment indicated as centimeters below sea floor (cmbsf) at the Pine Island (purple rectangles) and Thwaites (green circles) sites. The dashed line indicates the sediment-water interface, and the point at −0.5 cm represents the overlying bottom water sample. The inset in the Fe plot shows the low concentration gradient in the upper 4 cm at the Pine Island and Thwaites sites, and the insets in the Mn and Co plots show the low concentration peaks corresponding with Fe peaks in the upper 4 cm at the Pine Island site. Analytical error bars (± 1 σ) were smaller than the symbol size except for the lower concentrations of Mn (D). (For interpretation of the references to color in this figure legend, the reader is referred to the web version of this article.)

Table 1
Linear correlation coefficients (r; Pearson method) of pore water trace metal concentrations with Fe at the Pine Island and Thwaites sites. Significant correlations ≥0.8 are highlighted in bold.

Site	Al	Co	Mn	Y	Ti	Cd	Ni	Ba	Mo	P	U	V	Cr
Pine Island (Fe)	**0.99**	**0.99**	**0.91**	**0.9**	**0.8**	−0.07	0.4	−0.29	−0.39	0	−0.26	0.02	−0.14
Thwaites (Fe)	−0.12	0.6	0.46	0.65	−0.21	**0.83**	0.53	0.48	0.29	0.27	−0.02	−0.19	−0.63

<20 nM Ti) and exhibit no significant correlation with Fe or any other elements (Table 1; Supplemental Figs. 1, 2). Pore water Si also shows two concentration peaks in the PIG site of 125 μM and 123 μM at 0.5 and 2.5 cmbsf, respectively (Supplemental Fig. 2). At the TG site, pore water Si increases with depth to a maximum of 281 μM at 4 cmbsf and does not correlate with Fe, Al, or Ti (Supplemental Fig. 2).

Pore water Mn concentrations are below 200 nM throughout the PIG core and below 600 nM in the upper section of the TG core (Fig. 2D). Below 5 cmbsf at TG, Mn concentrations rise to a peak of 32 μM at 8 cmbsf. Concentrations of Mn decrease at 9 cmbsf, and then rise again downcore to maximum values of 58 μM. Concentrations of Co and Ni covary with Mn distributions in both cores, but at concentrations two to three orders of magnitude lower than Mn (~0.2–80 nM; Fig. 2E, F).

Distributions of U in the pore water exhibit divergent behavior at the two sites, decreasing from 14.7 nM in the overlying water at both sites (slightly above mean seawater values of ~13.2 ± 0.3 nM for salinity = 34; Owens et al., 2011) to 9.3 nM at the TG site and increasing to 23.2 nM at the PIG site (Supplemental Fig. 3G). Concentration profiles of pore water V and Cr profiles showed behavior similar to U (Supplemental Fig. 3F, H). Concentrations of V increased from seawater values (35–45 nM; Emerson and Huested, 1991) to a maximum of 62 nM at 3 cmbsf at PIG, while at TG concentrations decreased to a minimum of 14 nM at 8 cmbsf. Pore water Cr concentrations increase rapidly between 2 and 2.5 cmbsf at the PIG site, from ~9 nM to 26 nM, and at the TG site Cr decreases steadily to 1.2 nM at depth. Average concentrations of pore water Cd are slightly higher at PIG (3.3 nM) than at TG (2.3 nM), but with a single broad peak of 5 nM at 7 cmbsf at TG (Supplemental Fig. 3C). Barium increases downcore at both sites from ~100 nM to 150–200 nM, with generally higher concentrations at TG. The profile of Y at PIG shows peaks similar to those of Fe, Al, and Ti, but the overall profiles at the two sites resemble those of Ba. Pore water Mo and P concentrations are generally lower at TG, but otherwise show modest and non-systematic variations downcore (Supplemental Fig. 3D, E).

3.2. Sediment characteristics

At the PIG site, porosity in the surface sample is 0.82, and the surface porosity at the TG site is 0.88 (Supplemental Fig. 4A). Total organic carbon (TOC) is overall lower at the PIG site, ranging from 0.16 to 0.43 wt%, than at the Thwaites site, which has a range of 0.52–0.81 wt% (Supplemental Fig. 4B).

3.2.1. Solid Fe and Mn distribution and reactivity

The results of the sequential extraction can provide insight into the distribution of solid Fe and Mn phases in these sediments, with several important caveats. The hydroxylamine HCl extraction was designed to target carbonates, acid-volatile sulfide, and less crystalline Fe oxides such as ferrihydrite and lepidocrocite, while the dithionite extraction

targets crystalline Fe-oxides such as goethite and hematite (Poulton and Canfield, 2005). The extraction procedure used here has been tested extensively for the extraction of Fe minerals, but not of Mn minerals. Without using a procedure more specific to Mn, we hypothesize that the Mn phases extracted in each step may be similar to the Fe phases (carbonate and amorphous oxides in the hydroxylamine HCl and crystalline oxides in the dithionite). Importantly, many studies have highlighted that, even for Fe, these extraction steps are not specific in mineralogically complex natural sediments; for example, both steps are likely to dissolve some Fe-bearing clay minerals and dithionite is known to extract magnetite (Henkel et al., 2016; Hepburn et al., 2020; Köster et al., 2021; Ryan et al., 2008; Schröder et al., 2016; Vosteen et al., 2022). Therefore, to avoid assumptions of mineralogical specificity we define the hydroxylamine fraction as "easily reducible" and the dithionite fraction as "reducible" in this study, with the sum of the two fractions representing "reactive" Fe or Mn.

At the PIG site, little downcore variation is observed for Mn in any of the three solid fractions (Fig. 3A). The easily reducible fraction is larger than the reducible fraction, making up 19–44% of the total content, while the reducible fraction contributes 0.4–6% to the total. In contrast, at the TG site, the total content and easily reducible fractions are higher than at PIG in the upper 4 cm of sediment, with a peak of 42 μmol g^{-1} at 2.0–2.5 cmbsf for the total content and 26 μmol g^{-1} for the easily reducible fraction (Fig. 3B). The reducible fraction does not show the same vertical profile shape but makes up a larger percentage of the total Mn (5–16%) than at the PIG site.

No significant downcore trends are observed in the solid phase Fe contents at either site (Fig. 3C, D). Total Fe contents are slightly higher at the PIG sites with more downcore variability (average of 839 ± 86 μmol g^{-1}) than at the TG site (average of 767 ± 61 μmol g^{-1}). The easily reducible fractions are similar at both sites, making up 6–12% of the total Fe content, and the reducible fraction was larger than the easily reducible fraction at both sites.

3.3. Grain size and mineralogy

The grain size distributions are similar between the two sites, with the exception of a > 100 μm mode that is present only in the PIG site (Fig. 4A, C). At the PIG site, these >100 μm grains are most prevalent in sandy layers in the upper part of the core and decrease downcore in parallel with an increase in the 4–5 μm grain size (Fig. 4B). The TG site shows a sandy layer (more >100 μm grains and fewer 4–5 μm grains) at 5–7 cm depth, but no consistent downcore trend in grain size (Fig. 4D).

The smear slide analyses confirm the grain size distributions but also reveal the mineralogical compositions of individual grains. At both the TG and PIG sites, the dominant 4–5 μm mode consists primarily of terrigenous grains presumed to be quartz (Fig. 5A-D). In sediment cores from this region, this grain-size mode and mineralogy has been associated with transport and deposition by subglacial meltwater plumes (Lepp et al., 2022). High relief of grains in the ≤1 μm fraction may indicate heavy or magnetic minerals (e.g., magnetite; Fig. 5F). The >100 μm mode, which is much more abundant at the PIG site, is composed of grains with varying mineralogy, but includes an abundance of volcanic glass grains (Fig. 5A, B). These grains exhibit conchoidal fractures typical for glassy minerals and vesicle features suggestive of gas release during glass formation (e.g., cooling; Fig. 5E-G). The smear slides further indicate that the PIG core is barren of diatoms and diatom fragments below 3 cm; above 3 cm, diatoms (~40–60 μm) and diatom fragments (~20 μm) are present but quite sparse (<5 per slide). In contrast, diatoms and diatom fragments are more abundant throughout the sampled interval at the TG site.

3.3.1. Volcanic glass distribution and composition in the Pine Island sediments

Based on SEM-EDS analysis, the PIG volcanic glass grains have an average Fe/Al ratio of 0.41 ± 0.051 (mol/mol), an average Fe/Ti of 4.8 ± 0.28, and an average Fe/Si ratio of 0.19 ± 0.019 (Table 2). This glass Fe/Al value is almost double the typical ratio for upper continental crust

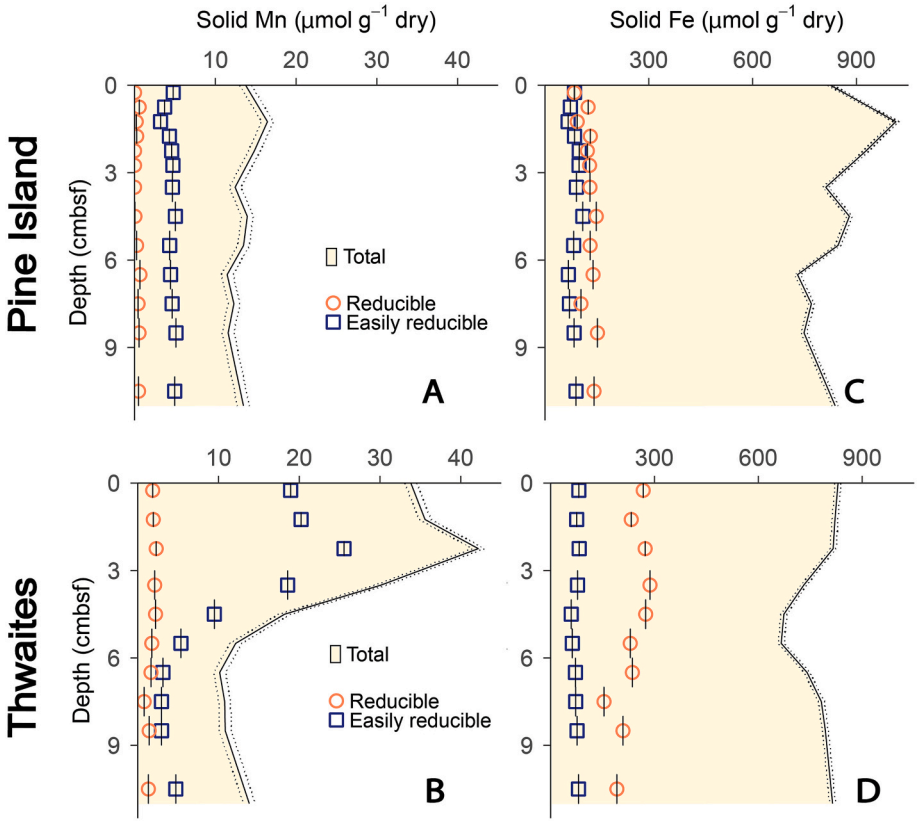

Fig. 3. Depth profiles of solid phase Mn and Fe contents at the Pine Island (A, C) and Thwaites (B, D) sites in μmol per g dry weight. Total contents are shown in the yellow shaded area, with the hash marks indicating analytical error in the measurement (± 1 σ). The easily reducible fraction is shown in blue squares, and the reducible fraction is shown in orange circles. Analytical error bars are smaller than the symbol size. Vertical bars indicate the range of depth interval over which each sediment sample was homogenized. (For interpretation of the references to color in this figure legend, the reader is referred to the web version of this article.)

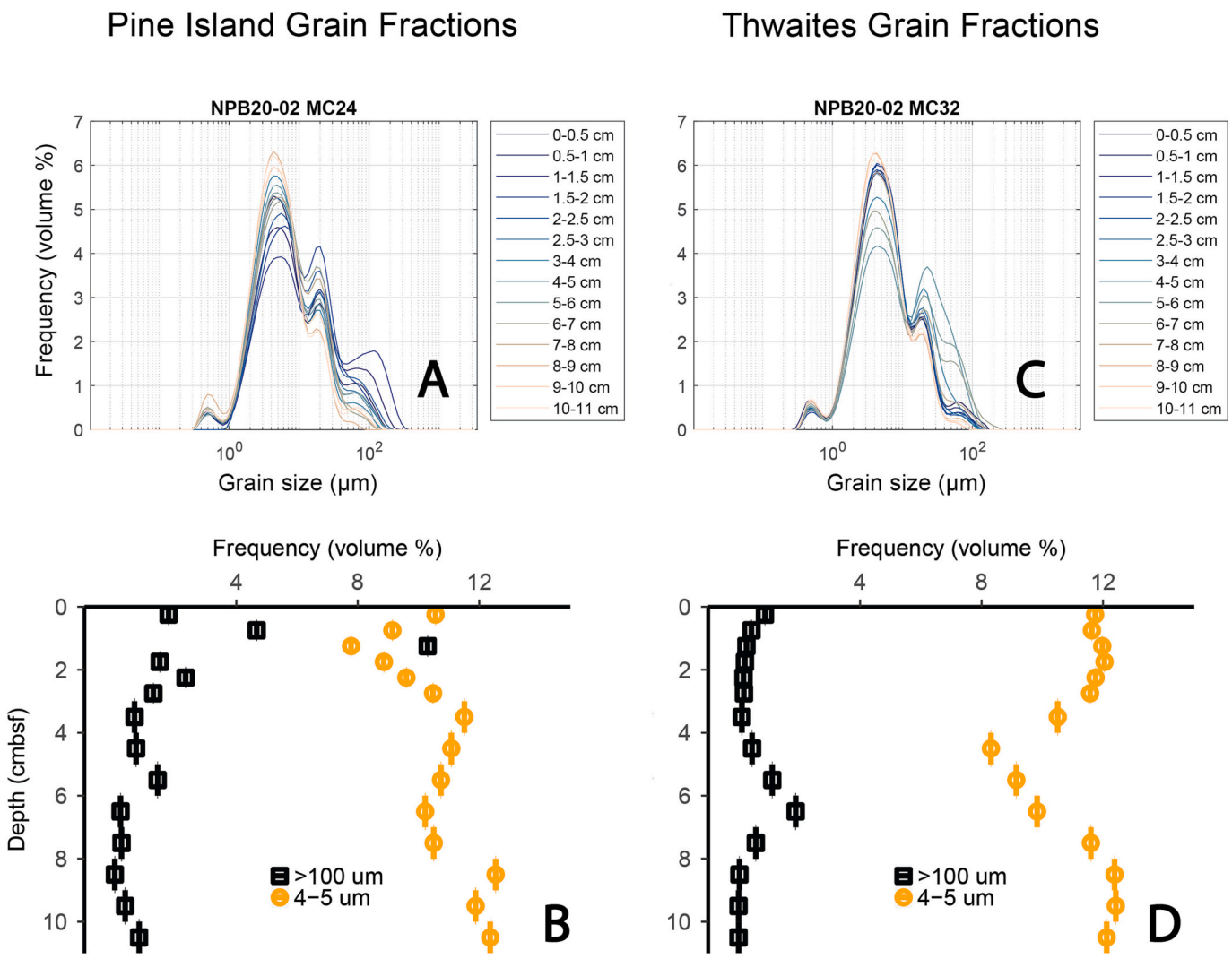

Fig. 4. Frequency distribution of grain size (μm) plotted on a log axis at the Pine Island (A) and Thwaites (C) sites, with the color of the line indicating the depth in the sediment (warmer colors = deeper, cooler colors = shallower). Depth profiles of the 4–5 um (orange circles) and > 100 um (black squares) grain size fractions at the Pine Island (B) and Thwaites (D) sites. Vertical bars indicate the depth interval over which each sediment sample was homogenized.

(~0.23), while the Fe/Ti is lower than typical crustal values (~8.8) (Rudnick and Gao, 2013). The glass Fe/Si ratio is about three times the typical crustal Fe/Si (~0.063). The glass composition is therefore easily distinguishable from other typical crustal values. The volume fraction of total volcanic grains >63 μm varies downcore, with a peak of 0.3 at 1–1.5 cmbsf (Fig. 6). A secondary peak of 0.2 volume fraction appears at 4–5 cm depth in the core. The relative contribution of unaltered "pristine" glass to total volcanics varies from 71% to 89% (Fig. 6).

3.4. Iron flux calculations

Fluxes of dissolved Fe from the sediment to the bottom water are approximately 100 times higher at the PIG site compared to the TG site (Table 3), and are dependent on the assumed physico-chemical speciation of pore water Fe. The highest flux values are calculated when pore water Fe is assumed to be either Fe^{2+} or Fe^{3+}. If, alternatively, pore water Fe exists primarily as small organic complexes such as siderophores, the calculated flux is only 67% of the value for Fe^{2+}. For pore water Fe that exists as ≤0.15 μm colloids, estimated fluxes decrease with increasing particle radius, as determined by the Stokes-Einstein relation (Eq. 2). The flux of the largest colloids in the Rhizon filtrate (150 nm) is estimated to be only 0.4% of the Fe^{2+} flux. We discuss the potential sources of the Fe flux at the PIG site in Section 4.2.3.

4. Discussion

4.1. Dynamic glacial sediment delivery

The physical properties of the sediment at both the PIG and TG sites indicate non-steady state deposition of sediment from variable sources. The quartz-dominated 4–5 μm grain size mode, diagnostic for meltwater plume deposits (Lepp et al., 2022), and the co-occurrence of this meltwater mode with heavy minerals in the ≤1 μm fraction could reflect hydraulic sorting in subglacial channels or during transport away from the grounding line (Witus et al., 2014). This suggests that a major source of sediment at the two sites is derived from sediment-laden meltwater plumes originating from glacial melt, subglacial discharge, or resuspension at the grounding line (Lepp et al., 2022; Witus et al., 2014). Both sediment cores have layers of coarser-grained and more poorly sorted material, indicating depositional events and/or changes in sediment source. The PIG site experienced a major calving event weeks before core collection, so iceberg scraping (which has been observed in up to 500 m water depth in Antarctica; Barnes and Lien, 1988) could be possible. However, given that distinct sand layers are observed (Figs. 4 and 6) and the ^{210}Pb profile shows an exponential decrease with depth in the upper 5 cm (Supplemental Fig. 5), we consider it very unlikely that this sediment interval was mixed by iceberg scraping. The PIG sediments

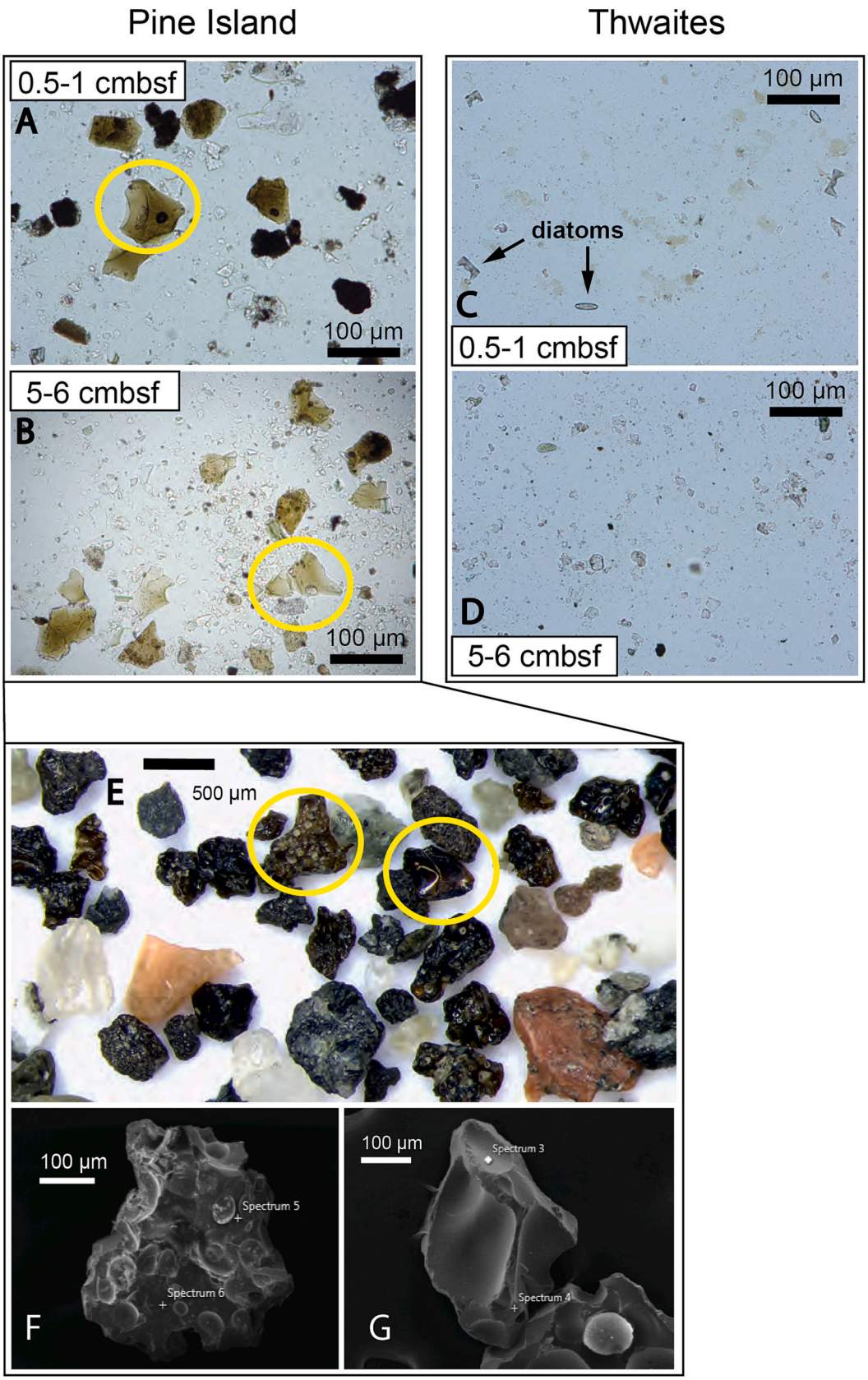

Fig. 5. Smear slide images of sediments from the Pine Island (A–B) and Thwaites (C–D) sites in the 0.5–1 cm and 5–6 cm intervals. Examples of pristine volcanic glass grains are identified in yellow circles. The >100 um fraction from 0 to 2 cmbsf at the Pine Island site is shown under reflected light in (E), and SEM images of two pristine volcanic glass grains from the same sample are shown in (F) and (G). (For interpretation of the references to color in this figure legend, the reader is referred to the web version of this article.)

Table 2
Elemental ratios (mol/mol) resulting from SEM-EDS analysis of volcanic glass in the Pine Island core (MC24). The sediment depth interval from which each grain was isolated is given. For grains from which two spectra were collected, ratios derived from each spectrum are separated by a comma. The mole % and weight percent of each element analyzed are given in Supplemental Table 2.

Depth interval of imaged grain (cmbsf)	Number of spectra per grain	Fe/Si (spectrum 1, spectrum 2)	Fe/Al (spectrum 1, spectrum 2)	Fe/Ti (spectrum 1, spectrum 2)
0–0.5	2	0.17, 0.21	0.37, 0.48	4.9, 4.8
0–0.5	2	0.16, 0.21	0.35, 0.48	4.5, 4.7
1.5–2	2	0.19, 0.18	0.41, 0.38	4.9, 4.5
1.5–2	2	0.23, 0.18	0.51, 0.41	5.0, –
2–2.5	2	0.18, 0.16	0.37, 0.37	4.7, 4.4
4–5	1	0.21	0.47	5.5
8–9	1	0.18	0.39	4.6
8–9	2	0.19, 0.18	0.40, 0.38	4.7, 4.7
Average ± 1 σ		0.19 ± 0.019	0.41 ± 0.051	4.8 ± 0.28

show a substantial >100 μm mode containing pristine volcanic glass grains that is not present at the TG site. In glaciomarine facies models, coarser grain sizes (i.e., sands and coarser) are typically associated with grounding line-proximal sediment deposition, often related to melt-out of basal debris (cf., Smith et al., 2019), so the glass-containing >100 μm mode at the PIG site is likely sourced from the nearby grounding line of the Pine Island Ice Shelf near the Hudson Mountains (see Fig. 1). At the PIG site, this mode is more prevalent in the upper layers of the core, suggesting that the deposition of glass-containing, >100 μm sediment at the grounding line has increased in recent years. Based on best estimates using ^{210}Pb profiles, the upper 10 cm interval sampled in this study is likely to have been deposited in the last 40 years for the PIG site (Comas et al., 2022) and the last 60 years for the TG site (Clark et al., 2023). Thus, the shift to increased supply of grounding line sediments at the PIG site has occurred over the last several decades, perhaps reflecting an increase in basal melting and grounding line retreat.

4.2. Pore water trace metal biogeochemistry

4.2.1. Reductive Fe release

In addition to differences in sediment sources and physical properties, pore water data from the PIG and TG sites indicate different geochemical reactions occurring at the two sites. The TG site shows distinctive characteristics of in situ reductive-oxidative (redox) cycling of Mn. Specifically, this site has an enrichment in easily reducible solid phase Mn in the upper 5 cm, directly overlying a substantial increase in pore water Mn concentration below 5 cmbsf. The dissolved Mn diffuses upward along its concentration gradient and, upon encountering sufficient oxygen in the overlying sediment and likely Mn-oxidizing bacteria, precipitates as authigenic Mn oxides (likely extracted in the easily reducible fraction of our sequential extraction; Burdige, 1993; Oldham et al., 2017; Herbert et al., 2020; Poulton and Canfield, 2005). If this process is sustained over time, the result is a Mn-oxide enrichment above the Mn-reduction zone as observed at the TG site (2–4 cmbsf; Fig. 3B).

The evidence for suboxic conditions and substantial Mn redox cycling below 5 cmbsf at the TG site is further supported by other trace metal evidence. For example, pore water concentrations of Co and Ni increase downcore along with Mn below this depth, and these elements are known to be released during Mn oxide reduction (Murray and Dillard, 1979; Peacock and Sherman, 2007; Stockdale et al., 2010). The total digest also revealed a surface enrichment in solid phase Mo, which is known to associate with Mn oxides (Supplemental Fig. 6) (Barling and Anbar, 2004; Shimmield and Price, 1986). The PIG site shows none of these indicators of reductive trace metal cycling over the sampled interval.

Further evidence for suboxic conditions at the TG site, in contrast to the PIG site, can be found in the pore water concentration of Cr, U, and

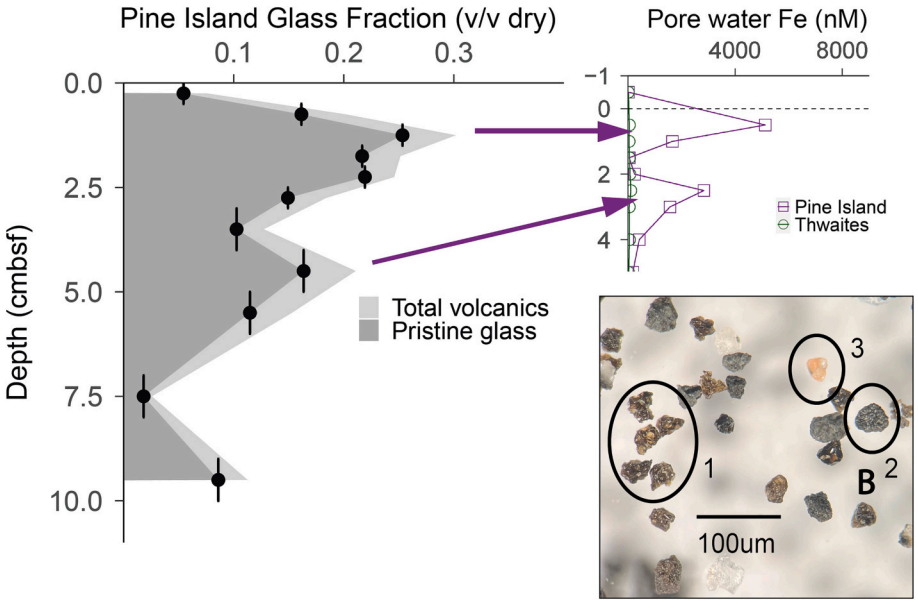

Fig. 6. Depth profile of the volume of total volcanic grains and of the subset of pristine glass grains, as a volume fraction of dry sediment in the Pine Island core (MC24; A). The dark gray shading and black circles indicate pristine glass grains, which are exemplified in circle 1, panel (B), similar to those shown in Fig. 5 F,G, while circle 2 shows a volcanic grain not classified as pristine, and circle 3 shows a grain classified as not volcanic (see Methods). The pore water Fe peaks corresponding to the volcanic glass peaks are indicated in the subpanel.

Table 3
Calculated fluxes of Fe, assuming soluble ionic, soluble organically complexed, and colloidal forms at the Pine Island and Thwaites sites. The diameter used to determine the diffusion coefficient for each particle size is given in parentheses. All units are μmol m^{-2} d^{-1}.

Site	Fe^{2+}	Fe^{3+}	Siderophore (1 nm)	Fresh ferrihydrite (30 nm)	General colloid (65 nm)	Large Fe colloid (150 nm)
Pine Island	17.1	15.5	11.5	0.382	0.176	0.0764
Thwaites	0.175	0.159	0.117	0.00392	0.00181	0.000783

V, which all increase with core depth at the PIG site and decrease downcore at the TG site (Supplemental Fig. 3). Globally, Cr is released to the ocean during oxidative weathering of continental crust and removed from seawater in suboxic and anoxic marine sediments through strong organic complexation of Cr(III) and adsorption onto particles (Fendorf, 1995; Gueguen et al., 2016). Under oxic, pH >7 conditions, Cr is most stable in the soluble, highly mobile Cr(VI) state (Kotas and Stasicka, 2000). Uranium is removed from pore water in anoxic sediments when U (VI) is reduced to U(IV) (catalyzed by anaerobic bacteria; Lovley et al., 1993) and precipitates as an insoluble phase (Klinkhammer and Palmer, 1991; Morford et al., 2009). In oxic seawater, V(V) is stable and soluble, but upon introduction of suboxic or anoxic conditions, V(V) is reduced to V(IV) and V(III) which are readily removed from solution through complexation and adsorption to particles or precipitation of insoluble hydroxide phases (Huang et al., 2015; Sadiq, 1988). Thus, the progressive decrease of pore water Cr, U, and V with depth at TG indicates suboxic conditions deeper in the sediment, while, in contrast, the accumulation of these three elements in the pore water at the PIG site indicates an absence of metal-reducing conditions. Without nitrate data, it is difficult to determine whether the upper 10 cm in the PIG sediments are truly oxic; oxygen could be depleted enough to allow denitrification over this interval. However, the trace metal profiles show no evidence of substantial metal redox cycling; we therefore conclude that this sediment interval is nonreductive with respect to Fe and Mn.

The development of Mn-reducing conditions at the TG site and not at the PIG site is attributable to the TG site being located under more open, productive water while the PIG site was until recently covered by the Pine Island Ice shelf. The TG sediments contain higher TOC content (~0.7 wt%) relative to the PIG site (~0.3 wt%) (Supplemental Fig. 4). The TG sediments also contain a higher abundance of diatoms, suggesting that some portion of the organic carbon was relatively labile (Fig. 5). Higher availability of labile organic matter drives higher rates of microbial respiration and more rapid drawdown of oxygen in the pore water (Froelich et al., 1979).

Despite evidence for suboxic Mn cycling at the TG site, the Fe fluxes across the sediment-water interface at both sites appear to be driven by nonreductive processes. In contrast to Mn, there is no evidence of sustained reductive Fe cycling at either site; no resolvable authigenic enrichments in solid phase Fe are observed, even in the easily reducible fraction which would be dominated by authigenic oxide precipitation. The pore water release of Fe below 5 cmbsf at the TG site (Fig. 2) may be incidental with Mn oxide dissolution, as Mn oxides typically contain significant amounts of Fe (Manceau et al., 1992), or concurrent low-level reduction of Fe oxides. The low Fe flux at this site results from the low pore water concentrations in the upper 1–2 cm. The source of the pore water Fe in the upper 5 cm at the TG is unlikely to be reductive as the sediments show no evidence of metal reduction in the upper few cm, and may instead be sourced from organic matter remineralization or submarine mineral weathering.

4.2.2. Evidence for significant nonreductive Fe release

There is no evidence of reductive metal cycling anywhere in the sampled sediment at the PIG site. However, the calculated flux of Fe across the sediment-water interface is 100× higher at PIG than at the TG core site. This flux is driven by a narrow peak in concentration just below the sediment surface, which is repeated in a second peak a few cm below. Both peaks are defined by at least two adjacent data points and there is no evidence of contamination in other trace metal profiles (Fig. 2; Supplemental Fig. 3). The Fe release to the pore water at the PIG site correlates closely with release of Al, Ti, and Si (Table 1; Supplemental Fig. 1). These elements are not redox-sensitive. Therefore, their release to the pore water indicates nonreductive dissolution of a lithogenic mineral phase. Assuming the pore water Fe is released by a mechanism common to these four elements, the pore water Fe concentrations and calculated flux across the sediment-water interface must be generated through nonreductive release during submarine weathering. Recent studies have indicated the importance of nonreductive release as a source of Fe to the ocean (Conway and John, 2014; Homoky et al., 2021; König et al., 2021; Radic et al., 2011), and our findings suggest substantial nonreductive release in the PIG sediments.

4.2.3. Volcanic source for Fe, Ti, and Al enrichment in the pore water

The evidence presented here suggests a nonreductive source of Fe from a mineral phase that is present at the PIG site but not at the TG site. We propose that a candidate for this Fe source is pristine volcanic glass within the seabed sediment (Fig. 5). We observed this glass only at the PIG site (core MC24). Regarding the possible source area and transport process for the glass deposited at the PIG site, there seem to be only two feasible scenarios (keeping in mind that the PIG site was ice-shelf covered for many years before 2020): 1) Ice-shelf rafting or transport from the grounding line of Pine Island Glacier (implying that the glass originates from somewhere within the PIG catchment area), or 2) input from the grounded ice adjacent to the sample site (implying that the glass originates from the nearby Hudson Mts. region; Fig. 1). There is evidence for volcanism within the past few thousand years both under the PIG drainage basin and in the Hudson Mountains region (Loose et al., 2018; Corr and Vaughan, 2008). There are also active volcanoes elsewhere in West Antarctica, for example in Marie Byrd Land (e.g., Dunbar et al., 2021), but given that no macroscopically visible ash layers have been reported in marine sediment cores from elsewhere in the Amundsen Sea embayment (e.g., Witus et al., 2014; Lepp et al., 2022), we assume a more local volcanic source for the glass at the PIG site (i.e., the Hudson Mountains). The majority of the glass in the PIG core is pristine, with no indications of physical or chemical alteration. However, these pristine glass grains are interspersed with glass grains that seem partially or heavily weathered and have smoothed edges suggestive of physical abrasion during transport (Fig. 5). This mixture of volcanic grains suggests incorporation of material from multiple sources.

Volcanic glasses can dissolve readily in seawater at low temperatures and have been shown to produce Fe colloids, providing a potentially important source of mobile Fe to the ocean (Duggen et al., 2007; Homoky et al., 2013, 2011a; Jones and Gislason, 2008; Longman et al., 2022). This process is thought to involve quantitative or congruent dissolution of the glass matrix, with subsequent alteration layers only forming once secondary minerals become supersaturated in the surrounding solution, allowing precipitation on the remaining glass surfaces (Crovisier et al., 1987; Heřmanská et al., 2022; Morin et al., 2015; Wolff-Boenisch et al., 2004). Several studies have documented the rapid dissolution of basaltic glass with rates of 0.001 g m^{-2} d^{-1} in seawater at 3 °C (Crovisier et al., 1987) and 0.0258 g m^{-2} d^{-1} in 10% seawater at 16 °C (Morin et al., 2015). Although the dissolution of the pristine glass grains at the PIG site probably occurred at a lower rate given the present in situ seawater temperature of ca. +0.6 °C, we attribute the peaks in pore water Fe, Al, and Ti concentration to glass dissolution over the estimated 40-year time period covered by this sediment interval.

The hypothesis of volcanic glass as a source of nonreductive Fe release is supported by the downcore glass count profile (Fig. 6), which exhibits a general decrease downcore and a double-peaked structure in the upper 4 cmbsf, similar to the pore water Fe profile. This double-peaked structure is also reflected in the total trace metal contents in the solid phase (Ti, Cr, V, Ni, Cu, Co, Cd; Supplemental Fig. 6), which could correlate with the presence of glass enriched in these metals. The trace metals that reach maximum concentrations within the sediment at 1.5 and 4 cm core depth (i.e., the same depths as the glass content peaks) are mostly in the group of elements typically enriched in the mantle relative to continental crust (the so-called “compatible” elements, e.g. Fe, Ni, Ca), while the solid phase trace metals that have minima at those depths are typically depleted in the mantle (“incompatible” elements, e.g. U and Ba) (Hofmann, 1997; McDonough and Sun, 1995). The peaks in glass fraction and the trace metal data do not depth-correlate perfectly with the pore water Fe peaks; however, the pore water and sediment samples were collected from different subcores of the same mega-corer

deployment and using different methods. Since small-scale variability in the seafloor topography and variation in sample depth measurements are possible, profiles from two subcores would not necessarily be expected to align exactly on a cm scale.

Finally, the hypothesis that Fe is released from the glass at the PIG site is supported by the Fe/Al and Fe/Ti ratios of the glass grains determined from the SEM-EDS data (Fig. 7A, B). Assuming quantitative dissolution of the mineral source through congruent weathering, the gradients of the lines passing through the porewater analyses should reflect the Fe/Al and Fe/Ti of their source mineral. Most of the pore water Fe/Al and Fe/Ti ratios fall closer to the glass ratios than to typical crustal ratios (Fig. 7). Furthermore, the pore water Al and Ti profiles predicted on the basis of the pore water Fe concentration and the glass Fe/Al and Fe/Ti ratios, assuming quantitative glass dissolution, are similar to those observed, particularly at the lower concentrations (Fig. 7C, D). Assuming Si from glass dissolution is additive with buried overlying water Si concentration, the same is true for predicted Si concentration profiles, although modest dissolution of biogenic silica may supply additional pore water Si below the uppermost peak at the Pine Island site (Supplemental Fig. 2). Note that at the Thwaites site, the pore water Si profile is likely dominated by biogenic silica dissolution rather than glass dissolution, given that the pore water Si concentrations are higher (maximum 281 μM at TG vs 125 μm at PIG), do not correlate with Al and Ti concentration, and that a greater number of diatoms were observed in smear slides from TG compared to PIG (Fig. 5). As discussed previously, the Fe, Al, and Ti pore water concentrations at PIG site are likely to be impacted by removal mechanisms including adsorption to particles and diffusion away from the source layer. Additionally, the submarine weathering of glass is likely to lead to secondary mineral precipitation, including hydroxides and poorly ordered sheet silicates. The combination of all these processes is likely to remove each element at slightly different rates, which could explain the offset between the glass and pore water Fe/Al ratio (Fig. 7A, C) and the one porewater sample that exhibits significantly lower than expected Ti (Fig. 7B, D).

4.3. Volcanic glass as a source of Fe to the Pine Island polynya

With nonreductive release of Fe likely in the surface sediments at both the PIG and TG sites, any Fe transported across the sediment-water interface is presumably in a Fe(III) phase rather than the soluble Fe^{2+} form typically assumed in Fe flux calculations for reducing sediments. We calculated the Fe fluxes at both sites for a range of possible Fe species including Fe^{2+}, Fe^{3+}, and several possible non-ionic forms. In oxic seawater, the aqueous Fe pool contains a significant (37–51%) fraction in the colloidal size range (0.03–0.4 μm; Boye et al., 2010; Fitzsimmons and Boyle, 2014), either as organic complexes or inorganic colloidal minerals such as ferrihydrite (Wells et al., 1991). According to the Stokes-Einstein relation, in a non-turbulent system such as pore water, small particles should diffuse at rates that are an inverse function of radius; larger particles diffuse more slowly. Since we do not know the form of the "dissolved" (<0.15 μm) pore water Fe we measured in this study, we calculated diffusion coefficients based on the representative radii for feasible forms of Fe smaller than or equal to our operational filter pore size. Organic complexes such as siderophores are generally in

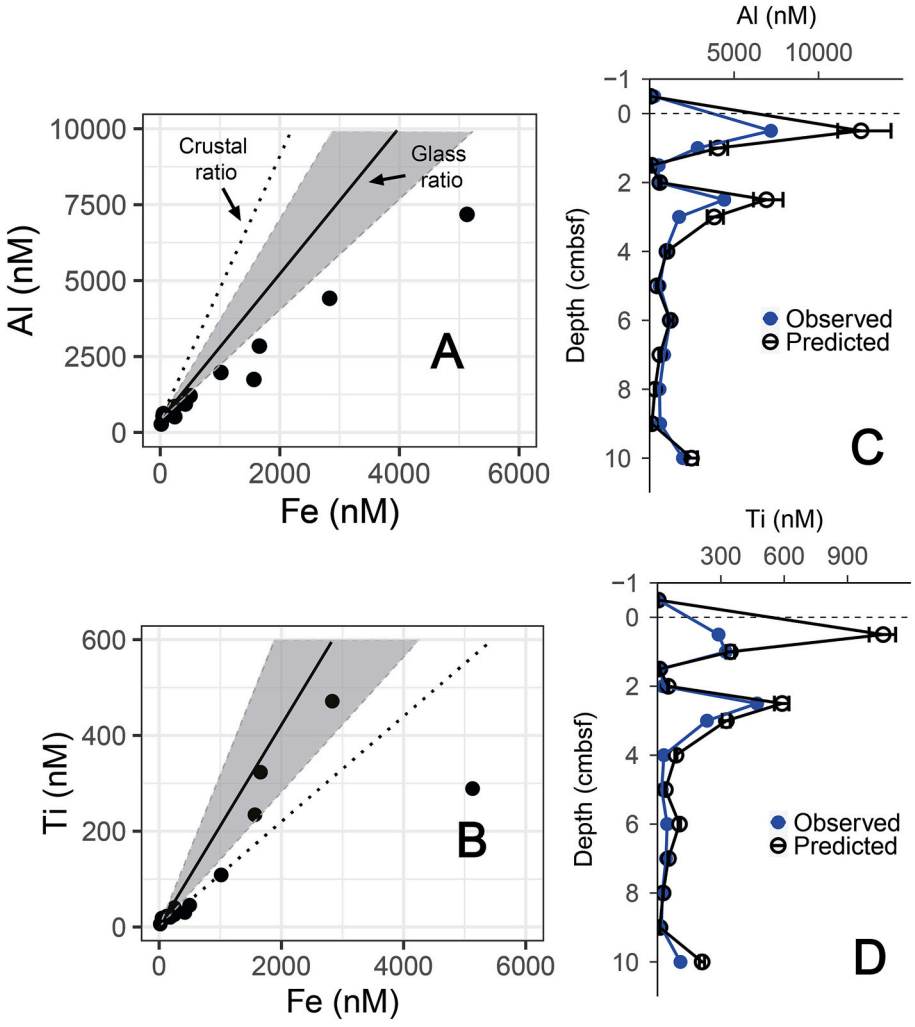

Fig. 7. Pore water Al (A) and Ti (B) plotted against Fe concentrations at the Pine Island site. The solid black line represents the elemental ratios of the glass grains. The gray shaded area indicates the error in the EDS analysis, based on the minimum and maximum ratios observed in the glass analysis. The black dashed line indicates the crustal ratios of Fe/Al (A) and Fe/Ti (B), with the slope of the line being equivalent to the ratio. Also shown are the observed depth profiles of pore water Al (C) and Ti (D) at the Pine Island site (solid blue dots), plotted alongside predicted values for Al and Ti (open black circles) based on the pore water Fe values using the Fe/Al and Fe/Ti ratios in the glass, assuming glass dissolution releases all elements to the pore water in proportion to their ratios in the glass. (For interpretation of the references to color in this figure legend, the reader is referred to the web version of this article.)

the size range of 140–1500 Da, or 0.7–1.5 nm assuming a typical protein density of 1.35 g/cm^3 (Baars et al., 2014; Vraspir and Butler, 2009) and fresh ferrihydrite colloids are thought to be around 30 nm (Wells et al., 1991). The grain size mode of general colloids in seawater was determined by flow field-flow fractionation as ~60–70 nm, and several studies have defined Fe colloids methodologically as the fraction of Fe between 30 and 200 nm (Boye et al., 2010; Vaillancourt and Balch, 2000). Therefore, we calculated fluxes for colloids with diameters of 65 nm and 150 nm to generally represent two possible characteristic fractions.

While no other study has considered Fe species size in determining benthic Fe fluxes, our range of potential Fe flux values (Table 3) fall within the range of other benthic Fe flux estimates in the Southern Ocean. Using bottom water concentration gradients and estimated vertical eddy diffusivity coefficients, benthic Fe fluxes of 1.3–16 μmol m^{-2} d^{-1} have been estimated in the Weddell and Scotia seas (De Jong et al., 2012), and 0.028–8.2 μmol m^{-2} d^{-1} in the Ross Sea (Marsay et al., 2014). Fluxes estimated using pore water Fe concentrations and assuming diffusive flux of reduced Fe^{2+} are generally higher, for example 2.4–43 μmol m^{-2} d^{-1} on the SW Antarctic Peninsula shelf (Burdige and Christensen, 2022), 52–171 μmol m^{-2} d^{-1} on the NW Antarctic Peninsula shelf to the South Orkney Islands (Baloza et al., 2022), and 3.8–420 μmol m^{-2} d^{-1} in Potter Cove, King George Island (Monien et al., 2014). A similar range of flux values has been determined in a variety of glaciated Arctic regions as well (Herbert et al., 2022, 2021; Vieira et al., 2018; Wehrmann et al., 2014).

Depending on the form of Fe diffusing across the sediment-water interface, the calculated flux could vary by three orders of magnitude or more, with the highest fluxes for the soluble ionic forms and the lowest fluxes for the large colloids (Table 3). It is therefore critical to clarify the size and forms of Fe present in the pore water in future studies of nonreductive benthic Fe flux. Net fluxes of Fe from the sediment to the water column are almost certainly impacted by multiple transport mechanisms in addition to molecular diffusion. Increases in bottom current speed (leading to resuspension), gravitational downslope transport processes, and bioturbation or bioirrigation by benthic organisms could inject particulate, colloidal, and truly dissolved ("soluble") forms of Fe into the bottom water at rates far above those driven by diffusion alone (Aller, 2004). In reducing sediments, where the predominant flux of Fe is presumed to be in the Fe^{2+} form, it is difficult to determine the fraction of Fe trapped through oxidation and precipitation at the oxic sediment surface, and estimates of flux based on diffusion along concentration gradients are likely to be overestimates (e.g., John et al., 2012). However, if Fe phases are introduced to the pore water through nonreductive mechanisms, as we argue for these cores, limited oxidative trapping at the surface will occur and the oxidized phases will be relatively stable in oxic seawater. For this reason, we believe our flux calculations presented here to be reasonable estimates of the true diffusive Fe flux for the given Fe speciation assumptions, with the total benthic Fe flux of all Fe phases possibly supplemented in situ by non-diffusive transport mechanisms.

Our estimated fluxes are based on only two sediment cores, making extrapolation to fluxes in the broader Amundsen Sea challenging. The pore water peak driving the high flux at the PIG core site may be transient, as suggested by the two narrow peaks at 0.5 and 2.5 cmbsf (Fig. 2). Without additional cores from the same area, it is difficult to estimate how significant a relatively large volcanic glass-driven flux might be in the regional sense. Furthermore, the large difference in sediment biogeochemistry and calculated benthic Fe fluxes between the PIG and TG core sites suggests that the rest of the seafloor in the Amundsen Sea is similarly variable. Because the distribution of macroscopic layers of volcanic ash in the Amundsen Sea embayment sediments seems to be geographically restricted to the northern part of inner Pine Island Bay, within ~75 km of the PIG sites studied here (C.-D. Hillenbrand, unpublished data), caution is warranted in upscaling our results from the PIG site to a broader spatial scale. On the other hand, dispersed volcanic glass could be widely distributed throughout the Amundsen Sea embayment, but may be present in highly diluted concentrations within the seabed sediments, and therefore not noted during visual inspection of the cores. The presence of even small quantities of glass in the sediments could still be biogeochemically important.

Regardless of broader flux values, however, the present study indicates that sediments are likely to be a net source of Fe to the Amundsen Sea bottom water. Given that both of our studied sites are in CDW inflow regions and depths (Wåhlin et al., 2021), these results broadly support the hypothesis that CDW flowing along the shelf acquires additional Fe from the seabed before entering the ice cavities in the eastern Amundsen Sea. This Fe-rich bottom water is transported to shallower water depths when it mixes with buoyant melt water in the ice cavity, providing a direct route for benthic Fe to reach the upper water column in the polynya (Sherrell et al., 2015; St-Laurent et al., 2019). Additionally, organically complexed and colloidal forms of Fe are more stable in seawater in ionic forms (Wells et al., 1991). Thus, the benthic Fe fluxes estimated in this study may fully or partially supply the micronutrient Fe required to sustain the phytoplankton bloom in the proximal Pine Island polynya.

5. Conclusion

Benthic fluxes of Fe from the seafloor to the overlying water column are likely driven by different processes at our two study sites near the Pine Island Glacier (PIG) and Thwaites Glacier (TG). The TG site is located further from the glacial sediment source in more frequently open-water marine conditions than is the PIG site, consistent with a greater accumulation of organic carbon in the sediments. This organic content drives reductive cycling of Mn below 5 cmbsf. Above this depth, the sediments show no evidence of metal reduction, and the low pore water Fe concentrations driving a small benthic flux are therefore likely to be nonreductive in source, despite the reducing conditions at greater depth at this site. In contrast, the core site in front of PIG was covered until a major calving event occurred in 2020, just before core collection. Our results show that, at this core site, Fe release to the pore water and flux across the sediment-water interface is driven by nonreductive dissolution of pristine volcanic glass abundant within the sediment core. This flux is roughly 100 times greater than at the TG site, suggesting that nonreductive glass dissolution could be an important source of Fe to the local bottom water. The volcanic source of this glass and its delivery mechanism are not yet certain, but the abundance of glass-rich sand appears to have increased at the PIG site during the last several decades, possibly related to acceleration of ice flow and enhanced grounding line retreat. If ongoing glacial retreat increases the delivery of volcanic glass to the seafloor, the local benthic Fe flux may increase concomitantly.

We demonstrate a novel method of determining nonreductive Fe fluxes using diffusion coefficients adjusted for the likely sizes of the pore water Fe phases. We show that with this consideration, the flux of Fe species other than soluble ions could be up to 1000× smaller than the flux calculated assuming the Fe is in soluble ionic (Fe^{2+} or Fe^{3+}) form. However, colloidal Fe phases produced through nonreductive weathering are stable in oxic seawater, and therefore more likely than aqueous ionic forms of Fe to be transported in the water column. The results presented here agree with previous findings that volcanogenic sediments are an important source of Fe to the global ocean, and further demonstrate that volcanic glass in coastal sediments could influence regional productivity patterns.

Further work is required to constrain flux values, identify mechanisms of Fe flux, and determine pathways by which benthic Fe may be transported to the euphotic zone in the Amundsen Sea. Future sediment sampling efforts in the area would benefit from investigating a broader spatial area and range of conditions in the Amundsen Sea, as well as gathering more information about the redox state of the sediment (including oxygen and nitrate data) and speciation of the pore water Fe (including ultrafiltration and ligand analysis). Additionally, future

studies should investigate the importance of other particulate and dissolved Fe sources including subglacial meltwater discharge, resuspension of sediments at the grounding line, and melt-out of debris from the ice-shelf base. Nevertheless, while the full range of variability in seafloor conditions is not yet known in the Amundsen Sea, our results show that nonreductive benthic Fe fluxes could be an important source of micronutrient Fe to the region. These results improve our understanding of how ongoing glacial retreat and climate change could alter the benthic Fe supply and impact the vibrant Amundsen Sea ecosystem.

Declaration of Competing Interest

The authors report that there are no competing interests to declare.

Data availability

All data published in this paper are included in the supplementary material.

Acknowledgements

This work is part of the ARTEMIS project, supported by the National Science Foundation Office of Polar Programs under award number 1941304 for R.M.S. It is based on collaborations and relies on samples from the Thwaites Offshore Research (THOR) project and the Geological History Constraints on the Magnitude of Grounding-Line Retreat in the Thwaites Glacier System project (GHC), which are both components of the International Thwaites Glacier Collaboration (ITGC; contribution number ITGC:095), with support from National Science Foundation (NSF; Grant No. 1738942 for J.S·W, subcontracted to L.M.S.) and Natural Environment Research Council (NERC; Grant No. NE/S006664/1). Additional funding for S.S. was provided by the National Science Foundation Division of Ocean Sciences (NSF; Grant No. 2124172). Salary and research support for L.C.H. was provided by the Earth, Ocean, and Atmospheric Sciences (EOAS) Postdoctoral Fellowship at Rutgers University and the National Science Foundation Office of Polar Programs Postdoctoral Research Fellowship (NSF; Grant No. 2212904). Stipend and research support for A.B. was provided by the Research Internships for Ocean Sciences (RIOS) NSF REU program at Rutgers University during the summer of 2022. We thank Dr. Kaixuan Bu for analyses performed in the Rutgers Inorganic Analytical Laboratory (RIAL) as well as all officers, crew, support staff and scientific personnel participating in the cruise NBP2002. Logistics were provided by the NSF-U.S. Antarctic Program and the NERC-British Antarctic Survey. All data presented in this paper are provided in the supplemental information.

Appendix A. Supplementary data

Supplementary data to this article can be found online at https://doi.org/10.1016/j.marchem.2023.104250.

References

Alderkamp, A.C., Van Dijken, G.L., Lowry, K.E., Connelly, T.L., Lagerström, M., Sherrell, R.M., Haskins, C., Rogalsky, E., Schofield, O., Stammerjohn, S.E., Yager, P. L., Arrigo, K.R., 2015. Fe availability drives phytoplankton photosynthesis rates during spring bloom in the Amundsen Sea Polynya, Antarctica. Elementa 3, 1–26. https://doi.org/10.12952/journal.elementa.000043.

Aller, R.C., 2004. Conceptual models of early diagenetic processes: the muddy seafloor as an unsteady, batch reactor. J. Mar. Res. 62, 815–835. https://doi.org/10.1357/0022240042880837.

Arndt, J.E., Larter, R.D., Friedl, P., Gohl, K., Höppner, K., Afanasyeva, V., et al., 2018. Bathymetric controls on calving processes at Pine Island Glacier. Cryosphere 12 (6), 2039–2050.

Arrigo, K.R., van Dijken, G.L., 2003. Phytoplankton dynamics within 37 Antarctic coastal polynya systems. J. Geophys. Res. Ocean. 108 https://doi.org/10.1029/2002jc001739.

Arrigo, K.R., van Dijken, G.L., Bushinsky, S., 2008. Primary production in the Southern Ocean, 1997-2006. J. Geophys. Res. Ocean. 113, 1997–2006. https://doi.org/10.1029/2007JC004551.

Arrigo, K.R., Lowry, K.E., van Dijken, G.L., 2012. Annual changes in sea ice and phytoplankton in polynyas of the Amundsen Sea, Antarctica. Deep Res. Part II Top. Stud. Oceanogr. 71–76, 5–15. https://doi.org/10.1016/j.dsr2.2012.03.006.

Baars, O., Morel, F.M.M., Perlman, D.H., 2014. ChemEx: isotope-assisted discovery of metal chelates in complex media using high-resolution LC-MS. Anal. Chem. 86, 11298–11305.

Baloza, M., Henkel, S., Geibert, W., Kasten, S., Holtappels, M., 2022. Benthic carbon remineralization and iron cycling in relation to sea ice cover along the eastern continental shelf of the Antarctic Peninsula. J. Geophys. Res. Ocean. 127 https://doi.org/10.1029/2021JC018401.

Barling, J., Anbar, A.D., 2004. Molybdenum isotope fractionation during adsorption by manganese oxides. Earth Planet. Sci. Lett. 217, 315–329. https://doi.org/10.1016/S0012-821X(03)00608-3.

Barnes, P.W., Lien, R., 1988. Icebergs rework shelf sediments to 500 m off Antarctica. Geology. 16 (12), 1130–1133.

Berelson, W., McManus, J., Coale, K., Johnson, K., Burdige, D., Kilgore, T., Colodner, D., Chavez, F., Kudela, R., Boucher, J., 2003. A time series of benthic flux measurements from Monterey Bay, CA. Cont. Shelf Res. 23, 457–481. https://doi.org/10.1016/S0278-4343(03)00009-8.

Boudreau, B.P., 1997. Diagenetic models and their implementation, Diagenetic Models and Their Implementation. Springer. https://doi.org/10.1016/s0264-8172(98)80005-6.

Boye, M., Nishioka, J., Croot, P., Laan, P., Timmermans, K.R., Strass, V.H., Takeda, S., de Baar, H.J.W., 2010. Significant portion of dissolved organic Fe complexes in fact is Fe colloids. Mar. Chem. 122, 20–27. https://doi.org/10.1016/j.marchem.2010.09.001.

Burdige, D.J., 1993. The biogeochemistry of manganese and iron reduction in marine sediments. Earth Sci. Rev. 35, 249–284. https://doi.org/10.1016/0012-8252(93)90040-E.

Burdige, D.J., Christensen, J.P., 2022. Iron biogeochemistry in sediments on the western continental shelf of the Antarctic Peninsula. Geochim. Cosmochim. Acta 326, 288–312. https://doi.org/10.1016/j.gca.2022.03.013.

Canfield, D.E., 1989. Reactive iron in marine sediments. Geochim. Cosmochim. Acta 53, 619–632.

Choi, A., Cho, H., Kim, S.H., Thamdrup, B., Lee, S.H., Hyun, J.H., 2016. Rates of N2 production and diversity and abundance of functional genes associated with denitrification and anaerobic ammonium oxidation in the sediment of the Amundsen Sea Polynya, Antarctica. Deep Res. Part II Top. Stud. Oceanogr. 123, 113–125. https://doi.org/10.1016/j.dsr2.2015.07.016.

Clark, R.W., Wellner, J.S., Hillenbrand, C.D., Totten, R.L., Smith, J.A., Simkins, L.M., Larter, R.D., Hogan, K.A., Graham, A.G.C., Nitsche, F.O., Lehrmann, A.A., Lepp, A.P., Kirkham, J.D., Fitzgerald, V.T., Garcia-Barrera, G., Ehrmann, W., Wacker, L., 2023. Synchronous retreat of Thwaites and Pine Island glaciers in response to external forcings in the pre-satellite era. PNAS. In press.

Comas, M.M., Wellner, J., Hillenbrand, C.-D., Clark, R.W., Smith, J., Larter, R.D., Graham, A.G.C., Hogan, K., Nitsche, F.O., Totten, R.L., Anderson, J.B., Simkins, L.M., Lehrmann, A., Lepp, A., Mawbey, E., Hopkins, B., Marschalek, J., 2022. Sedimentary Record of Pre-Satellite Retreat of Pine Island Glacier, Amundsen Sea, Antarctica. In: Poster C32E-0878. AGU Fall Meeting 2022, 14 December 2022, Chicago, IL.

Conway, T.M., John, S.G., 2014. Quantification of dissolved iron sources to the North Atlantic Ocean. Nature 511, 212–215. https://doi.org/10.1038/nature13482.

Corr, H.F.J.C., Vaughan, D.G., 2008. A recent volcanic eruption beneath the West Antarctic ice sheet. Nature 1, 122–125.

Crovisier, J.L., Honnorez, J., Eberhart, J.P., 1987. Dissolution of basaltic glass in seawater: mechanism and rate. Geochim. Cosmochim. Acta 51, 2977–2990. https://doi.org/10.1016/0016-7037(87)90371-1.

Dale, A.W., Nickelsen, L., Scholz, F., Hensen, C., Oschlies, A., Wallmann, K., 2015. A revised global estimate of dissolved iron fluxes. Glob. Biogeochem. Cycles 29, 691–707. https://doi.org/10.1002/2014GB005017.Received.

De Jong, J., Schoemann, V., Lannuzel, D., Croot, P., De Baar, H., Tison, J.L., 2012. Natural iron fertilization of the Atlantic sector of the Southern Ocean by continental shelf sources of the Antarctic Peninsula. J. Geophys. Res. Biogeosci. 117 https://doi.org/10.1029/2011JG001679.

DeConto, R.M., Pollard, D., Alley, R.B., Velicogna, I., Gasson, E., Gomez, N., et al., 2021. The Paris Climate Agreement and future sea-level rise from Antarctica. Nature. 593 (7857), 83–89. https://doi.org/10.1038/s41586-021-03427-0.

Dickens, G.R., Koelling, M., Smith, D.C., Schnieders, L., 2007. Rhizon sampling of pore waters on scientific drilling expeditions: an example from the IODP expedition 302, Arctic Coring Expedition (ACEX). Sci. Drill. 4, 22–25. https://doi.org/10.2204/iodp.sd.4.08.2007.

Dinniman, M.S., St-Laurent, P.S., 2020. Analysis of iron sources in Antarctic Continental Shelf Waters. J. Geophys. Res. Oceans 1–19. https://doi.org/10.1029/2019JC015736.

Duggen, S., Croot, P., Schacht, U., Hoffmann, L., 2007. Subduction zone volcanic ash can fertilize the surface ocean and stimulate phytoplankton growth: evidence from biogeochemical experiments and satellite data. Geophys. Res. Lett. 34, 1–5. https://doi.org/10.1029/2006GL027522.

Dunbar, N.W., Iverson, N.A., Smellie, J.L., McIntosh, W.C., Zimmerer, M.J., Kyle, P.R., 2021. Chapter 7.4: active volcanoes on Marie Byrd Land. Geol. Soc. Lond. Mem. 55 (1), 759. https://doi.org/10.1144/M55-2019-29.

Elrod, V.A., Berelson, W.M., Coale, K.H., Johnson, K.S., 2004. The flux of iron from continental shelf sediments: a missing source for global budgets. Geophys. Res. Lett. 31, 2–5. https://doi.org/10.1029/2004GL020216.

Emerson, S.R., Huested, S.S., 1991. Ocean anoxia and the concentrations of molybdenum and vanadium in seawater. Mar. Chem. 34, 177–196.
Favier, L., Durand, G., Cornford, S.L., Gudmundsson, G.H., Gagliardini, O., Gillet-Chaulet, F., Le Brocq, A.M., 2014. Retreat of Pine Island Glacier controlled by marine ice-sheet instability. Nat. Clim. Change. 4 (2), 117–121.
Fendorf, S.E., 1995. Surface reactions of chromium in soils and waters. Geoderma 67, 55–71.
Fitzsimmons, J.N., Boyle, E.A., 2014. Both soluble and colloidal iron phases control dissolved iron variability in the tropical North Atlantic Ocean. Geochim. Cosmochim. Acta 125, 539–550. https://doi.org/10.1016/j.gca.2013.10.032.
Froelich, P.N., Klinkhammer, G.P., Bender, M.L., Luedtke, N.A., Heath, G.R., Cullen, D., Dauphin, P., Hammond, D., Hartman, B., 1979. Early oxidation of organic matter in pelagic sediments of the eastern equatorial Atlantic: suboxic diagenesis. Geochim. Cosmochim. Acta 43, 1075–1090.
Greisman, P., 1979. On upwelling driven by the melt of ice shelves and tidewater glaciers. Deep Sea Res. Part A Oceanogr. Res. Pap. 26, 1051–1065. https://doi.org/10.1016/0198-0149(79)90047-5.
Gueguen, B., Reinhard, C.T., Algeo, T.J., Peterson, L.C., Nielsen, S.G., Wang, X., Rowe, H., Planavsky, N.J., 2016. The chromium isotope composition of reducing and oxic marine sediments. Geochim. Cosmochim. Acta 184, 1–19. https://doi.org/10.1016/j.gca.2016.04.004.
Hatta, M., Measures, C.I., Selph, K.E., Zhou, M., Hiscock, W.T., 2013. Iron fluxes from the shelf regions near the South Shetland Islands in the Drake Passage during the austral-winter 2006. Deep Res. Part II Top. Stud. Oceanogr. 90, 89–101. https://doi.org/10.1016/j.dsr2.2012.11.003.
Hatta, M., Measures, C.I., Lam, P.J., Ohnemus, D.C., Auro, M.E., Grand, M.M., Selph, K. E., 2017. The relative roles of modified circumpolar deep water and benthic sources in supplying iron to the recurrent phytoplankton blooms above Pennell and Mawson Banks, Ross Sea, Antarctica. J. Mar. Syst. 166, 61–72. https://doi.org/10.1016/j.jmarsys.2016.07.009.
Henkel, S., Kasten, S., Poulton, S.W., Staubwasser, M., 2016. Determination of the stable iron isotopic composition of sequentially leached iron phases in marine sediments. Chem. Geol. 421, 93–102. https://doi.org/10.1016/j.chemgeo.2015.12.003.
Hepburn, L.E., Butler, I.B., Boyce, A., Schröder, C., 2020. The use of operationally-defined sequential Fe extraction methods for mineralogical applications: a cautionary tale from Mössbauer spectroscopy. Chem. Geol. 543 (September 2019), 119584 https://doi.org/10.1016/j.chemgeo.2020.119584.
Herbert, L.C., Riedinger, N., Michaud, A.B., Laufer, K., Røy, H., Jørgensen, B.B., Heilbrun, C., Aller, R.C., Cochran, J.K., Wehrmann, L.M., 2020. Glacial controls on redox-sensitive trace element cycling in Arctic fjord sediments (Spitsbergen, Svalbard). Geochim. Cosmochim. Acta 271, 33–60. https://doi.org/10.1016/j.gca.2019.12.005.
Herbert, L.C., Zhu, Q., Michaud, A.B., Laufer-Meiser, K., Jones, C.K., Riedinger, N., Stooksbury, Z.S., Aller, R.C., Jørgensen, B.B., Wehrmann, L.M., 2021. Benthic iron flux influenced by climate-sensitive interplay between organic carbon availability and sedimentation rate in Arctic fjords. Limnol. Oceanogr. 66, 3374–3392. https://doi.org/10.1002/lno.11885.
Herbert, L.C., Michaud, A.B., Laufer-Meiser, K., Hoppe, C.J.M., Zhu, Q., Aller, R.C., Jørgensen, B.B., Wehrmann, L.M., 2022. Tight benthic-pelagic coupling drives seasonal and interannual changes in iron-sulfur cycling in Arctic fjord sediments (Kongsfjorden, Svalbard). J. Mar. Syst. 225 https://doi.org/10.1016/j.jmarsys.2021.103645.
Heřmanská, M., Voigt, M.J., Marieni, C., Declercq, J., Oelkers, E.H., 2022. A comprehensive and internally consistent mineral dissolution rate database: Part I: Primary silicate minerals and glasses. Chem. Geol. 597. https://doi.org/10.1016/j.chemgeo.2022.120807.
Hoffman, M.J., Asay-Davis, X., Price, S.F., Fyke, J., Perego, M., 2019. Effect of subshelf melt variability on sea level rise contribution from Thwaites Glacier, Antarctica. J. Geophys. Res. Earth Surf. 124, 2798–2822. https://doi.org/10.1029/2019JF005155.
Hofmann, A.W., 1997. Mantle geochemistry: the message from oceanic volcanism. Nature 385, 219–229.
Homoky, W.B., Hembury, D.J., Hepburn, L.E., Mills, R.A., Statham, P.J., Fones, G.R., Palmer, M.R., 2011a. Iron and manganese diagenesis in deep sea volcanogenic sediments and the origins of pore water colloids. Geochim. Cosmochim. Acta 75, 5032–5048. https://doi.org/10.1016/j.gca.2011.06.019.
Homoky, W.B., Hembury, D.J., Hepburn, L.E., Mills, R.A., Statham, P.J., Fones, G.R., Palmer, M.R., 2011b. Iron and manganese diagenesis in deep sea volcanogenic sediments and the origins of pore water colloids. Geochim. Cosmochim. Acta 75, 5032–5048. https://doi.org/10.1016/j.gca.2011.06.019.
Homoky, W.B., Severmann, S., McManus, J., Berelson, W.M., Riedel, T.E., Statham, P.J., Mills, R.A., 2012. Dissolved oxygen and suspended particles regulate the benthic flux of iron from continental margins. Mar. Chem. 134–135, 59–70. https://doi.org/10.1016/j.marchem.2012.03.003.
Homoky, W.B., John, S.G., Conway, T.M., Mills, R.A., 2013. Distinct iron isotopic signatures and supply from marine sediment dissolution. Nat. Commun. 4 https://doi.org/10.1038/ncomms3143.
Homoky, W.B., Weber, T., Berelson, W.M., Conway, T.M., Henderson, G.M., Van Hulten, M., Jeandel, C., Severmann, S., Tagliabue, A., 2016. Quantifying trace element and isotope fluxes at the ocean-sediment boundary: a review. Phil. Trans. R. Soc. A 374, 20160246. https://doi.org/10.1098/rsta.2016.0246.
Holland, P.R., Bracegirdle, T.J., Dutrieux, P., et al., 2019. West Antarctic ice loss influenced by internal climate variability and anthropogenic forcing. Nat. Geosci. 12, 718–724. https://doi.org/10.1038/s41561-019-0420-9.
Homoky, W.B., Conway, T.M., John, S.G., König, D., Deng, F.F., Tagliabue, A., Mills, R. A., 2021. Iron colloids dominate sedimentary supply to the ocean interior. Proc. Natl. Acad. Sci. U. S. A. 118 https://doi.org/10.1073/pnas.2016078118.
Huang, J.-H., Huang, F., Evans, L., Glasauer, S., 2015. Vanadium: Global (bio) geochemistry. Chem. Geol. 417, 68–89. https://doi.org/10.1016/J.CHEMGEO.2015.09.019.
Jenkins, A., Dutrieux, P., Jacobs, S., Steig, E.J., Gudmundsson, G.H., Smith, J., Heywood, K.J., 2016. Decadal ocean forcing and Antarctic ice sheet response: lessons from the Amundsen Sea. Oceanography 29, 106–117. https://doi.org/10.5670/oceanog.2016.103.
John, S.G., Mendez, J., Moffett, J., Adkins, J., 2012. The flux of iron and iron isotopes from San Pedro Basin sediments. Geochim. Cosmochim. Acta 93, 14–29. https://doi.org/10.1016/j.gca.2012.06.003.
Jones, M.T., Gislason, S.R., 2008. Rapid releases of metal salts and nutrients following the deposition of volcanic ash into aqueous environments. Geochim. Cosmochim. Acta 72, 3661–3680. https://doi.org/10.1016/j.gca.2008.05.030.
Kim, S.H., Choi, A., Jin Yang, E., Lee, S.H., Hyun, J.H., 2016. Low benthic respiration and nutrient flux at the highly productive Amundsen Sea Polynya, Antarctica. Deep Res. Part II Top. Stud. Oceanogr. 123, 92–101. https://doi.org/10.1016/j.dsr2.2015.10.004.
Klar, J.K., Homoky, W.B., Statham, P.J., Birchill, A.J., Harris, E.L., Woodward, E.M.S., Silburn, B., Cooper, M.J., James, R.H., Connelly, D.P., Chever, F., Lichtschlag, A., Graves, C., 2017. Stability of dissolved and soluble Fe (II) in shelf sediment pore waters and release to an oxic water column. Biogeochemistry 135, 49–67. https://doi.org/10.1007/s10533-017-0309-x.
Klinkhammer, G.P., Palmer, M.R., 1991. Uranium in the oceans: where it goes and why. Geochim. Cosmochim. Acta 55, 1799–1806.
König, D., Conway, T.M., Ellwood, M.J., Homoky, W.B., Tagliabue, A., 2021. Constraints on the cycling of Iron isotopes from a global ocean model. Glob. Biogeochem. Cycles 35, 1–23. https://doi.org/10.1029/2021GB006968.
Köster, M., Kars, M., Schubotz, F., Tsang, M.Y., Maisch, M., Kappler, A., et al., 2021. Evolution of (bio-)geochemical processes and diagenetic alteration of sediments along the tectonic migration of ocean floor in the Shikoku Basin off Japan. Geochem. Geophys. Geosyst. 22 (8), 1–25.
Kotas, J., Stasicka, Z., 2000. Chromium occurrence in the environment and methods of its speciation. Environ. Pollut. 107, 263–283.
Lepp, A.P., Simkins, L.M., Anderson, J.B., Clark, R.W., Wellner, J.S., Hillenbrand, C.-D., Smith, J.A., Lehrmann, A.A., Totten, R., Larter, R.D., Hogan, K.A., Nitsche, F.O., Graham, A.G.C., Wacker, L., 2022. Sedimentary signatures of persistent subglacial meltwater drainage from Thwaites Glacier, Antarctica. Front. Earth Sci. 10, 1–19. https://doi.org/10.3389/feart.2022.863200.
Longman, J., Palmer, M.R., Gernon, T.M., Manners, H.R., Jones, M.T., 2022. Subaerial volcanism is a potentially major contributor to oceanic iron and manganese cycles. Commun. Earth Environ. 3, 1–8. https://doi.org/10.1038/s43247-022-00389-7.
Loose, B., Naveira Garabato, A.C., Schlosser, P., Jenkins, W.J., Vaughan, D., Heywood, K. J., 2018. Evidence of an active volcanic heat source beneath the Pine Island glacier. Nat. Commun. 9 (1), 1–9. https://doi.org/10.1038/s41467-018-04421-3.
Lovley, D.R., 1993. Dissimilatory metal reduction. Annu. Rev. Microbiol. 47, 263–290. https://doi.org/10.1146/annurev.mi.47.100193.001403.
Lovley, D.R., Roden, E.E., Phillips, E.J.P., Woodward, J.C., 1993. Enzymatic iron and uranium reduction by sulfate-reducing bacteria. Mar. Geol. 113, 41–53.
Malczyk, G., Gourmelen, N., Goldberg, D., Wuite, J., Nagler, T., 2020. Repeat subglacial lake drainage and filling beneath Thwaites Glacier. Geophys. Res. Lett. 47 https://doi.org/10.1029/2020GL089658.
Manceau, A., Gorshkov, A.I., Drits, V.A., 1992. Structural chemistry of Mn, Fe, Co, and Ni in manganese hydrous oxides: Part II. Information from EXAFS spectroscopy and electron and X-ray diffraction. Am. Mineral. 77, 1144–1157.
Marsay, C.M., Sedwick, P.N., Dinniman, M.S., Barrett, P.M., Mack, S.L., McGillicuddy, D. J., 2014. Estimating the benthic efflux of dissolved iron on the Ross Sea continental shelf. Geophys. Res. Lett. 41, 7576–7583. https://doi.org/10.1002/2014GL061684.
McDonough, W.F., Sun, S.-s, 1995. The composition of the Earth. Chem. Geol. 120, 223–253.
Milillo, P., Rignot, E., Rizzoli, P., Scheuchl, B., Mouginot, J., Bueso-Bello, J., et al., 2019. Heterogeneous retreat and ice melt of Thwaites Glacier, West Antarctica. Sci. Adv. 5, eaau3433. https://doi.org/10.1126/sciadv.aau3433.
Monien, P., Lettmann, K.A., Monien, D., Asendorf, S., W. A.C, Lim, C.H., Thal, J., Schnetger, B., Brumsack, H.J., 2014. Redox conditions and trace metal cycling in coastal sediments from the maritime Antarctic. Geochim. Cosmochim. Acta 141, 26–44. https://doi.org/10.1016/j.gca.2014.06.003.
Morford, J.L., Martin, W.R., Carney, C.M., 2009. Uranium diagenesis in sediments underlying bottom waters with high oxygen content. Geochim. Cosmochim. Acta 73, 2920–2937. https://doi.org/10.1016/j.gca.2009.02.014.
Morin, G.P., Vigier, N., Verney-Carron, A., 2015. Enhanced dissolution of basaltic glass in brackish waters: impact on biogeochemical cycles. Earth Planet. Sci. Lett. 417, 1–8. https://doi.org/10.1016/j.epsl.2015.02.005.
Murray, J.W., Dillard, J.G., 1979. The oxidation of cobalt(II) adsorbed on manganese dioxide. Geochim. Cosmochim. Acta 43, 781–787. https://doi.org/10.1016/0016-7037(79)90261-8.
Noffke, A., Hensen, C., Sommer, S., Scholz, F., Bohlen, L., Mosch, T., Graco, M., Wallmann, K., 2012. Benthic iron and phosphorus fluxes across the Peruvian oxygen minimum zone. Limnol. Oceanogr. 57, 851–867. https://doi.org/10.4319/lo.2012.57.3.0851.
Oldham, V.E., Jones, M.R., Tebo, B.M., Luther, G.W., 2017. Oxidative and reductive processes contributing to manganese cycling at oxic-anoxic interfaces. Mar. Chem. 195, 122–128.

Oliver, H., St-Laurent, P., Sherrell, R.M., Yager, P.L., 2019. Modeling iron and light controls on the summer *Phaeocystis antarctica* bloom in the Amundsen Sea Polynya. Glob. Biogeochem. Cycles. https://doi.org/10.1029/2018GB006168.

Owens, S.A., Buesseler, K.O., Sims, K.W.W., 2011. Re-evaluating the 238U-salinity relationship in seawater: implications for the 238U-234Th disequilibrium method. Mar. Chem. 127, 31–39. https://doi.org/10.1016/j.marchem.2011.07.005.

Peacock, C.L., Sherman, D.M., 2007. Sorption of Ni by birnessite: equilibrium controls on Ni in seawater. Chem. Geol. 238, 94–106. https://doi.org/10.1016/j.chemgeo.2006.10.019.

Planquette, H., Sherrell, R.M., Stammerjohn, S., Field, M.P., 2013. Particulate iron delivery to the water column of the Amundsen Sea, Antarctica. Mar. Chem. 153, 15–30. https://doi.org/10.1016/j.marchem.2013.04.006.

Poulton, S.W., Canfield, D.E., 2005. Development of a sequential extraction procedure for iron: implications for iron partitioning in continentally derived particulates. Chem. Geol. 214, 209–221. https://doi.org/10.1016/j.chemgeo.2004.09.003.

Radic, A., Lacan, F., Murray, J.W., 2011. Iron isotopes in the seawater of the equatorial Pacific Ocean: new constraints for the oceanic iron cycle. Earth Planet. Sci. Lett. 306, 1–10. https://doi.org/10.1016/j.epsl.2011.03.015.

Randall-Goodwin, E., Meredith, M.P., Jenkins, A., Yager, P.L., Sherrell, R.M., Abrahamsen, E.P., Guerrero, R., Yuan, X., Mortlock, R.A., Gavahan, K., Alderkamp, A.C., Ducklow, H., Robertson, R., Stammerjohn, S.E., 2015. Freshwater distributions and water mass structurein the Amundsen Sea Polynya region, Antarctica. Elementa 3, 1–22. https://doi.org/10.12952/journal.elementa.000065.

Rignot, E., Mouginot, J., Scheuchl, B., 2011. Antarctic grounding line mapping from differential satellite radar interferometry. Geophys. Res. Lett. 38, L10504. https://doi.org/10.1029/2011GL047109.

Rowley, P.D., Laudon, T.S., LaPrade, K.E., LeMasurier, W.E., 1990. Hudson mountains. In: American Geophysical Union: Antarctic Research Series, 48, pp. 289–293.

Rudnick, R.L., Gao, S., 2013. Composition of the continental crust. In: Treatise on Geochemistry, 2nd ed. Elsevier Ltd. https://doi.org/10.1016/B978-0-08-095975 7.00301-6

Ryan, P.C., Hillier, S., Wall, A.J., 2008. Stepwise effects of the BCR sequential chemical extraction procedure on dissolution and metal release from common ferromagnesian clay minerals: a combined solution chemistry and X-ray powder diffraction study. Sci. Total Environ. 407 (1), 603–614. https://doi.org/10.1016/j.scitotenv.2008.09.019.

Sadiq, M., 1988. Thermodynamic solubility relationships of inorganic vanadium in the marine environment. Mar. Chem. 23, 87–96. https://doi.org/10.1016/0304-4203(88)90024-2.

Scambos, T.A., Bell, R.E., Alley, R.B., Anandakrishnan, S., Bromwich, D.H., Brunt, K., Christianson, K., Creyts, T., Das, S.B., DeConto, R., Dutrieux, P., Fricker, H.A., Holland, D., MacGregor, J., Medley, B., Nicolas, J.P., Pollard, D., Siegfried, M.R., Smith, A.M., Steig, E.J., Trusel, L.D., Vaughan, D.G., Yager, P.L., 2017. How much, how fast?: a science review and outlook for research on the instability of Antarctica's Thwaites Glacier in the 21st century. Glob. Planet. Change 153, 16–34. https://doi.org/10.1016/j.gloplacha.2017.04.008.

Schröder, C., Köhler, I., Muller, F.L.L., Chumakov, A.I., Kupenko, I., Rüffer, R., et al., 2016. The biogeochemical iron cycle and astrobiology. Hyperfine Interact. 237 (1), 1–14.

Seeberg-Elverfeldt, J., Schlüter, M., Feseker, T., Kölling, M., 2005. Rhizon sampling of porewaters near the sediment-water interface. Limnol. Oceanogr. Methods 3, 361–371.

Severmann, S., McManus, J., Berelson, W.M., Hammond, D.E., 2010. The continental shelf benthic iron flux and its isotope composition. Geochim. Cosmochim. Acta 74, 3984–4004. https://doi.org/10.1016/j.gca.2010.04.022.

Sherrell, R.M., Lagerström, M.E., Forsch, K.O., Stammerjohn, S.E., Yager, P.L., 2015. Dynamics of dissolved iron and other bioactive trace metals (Mn, Ni, cu, Zn) in the Amundsen Sea Polynya, Antarctica. Elementa 3, 1–27. https://doi.org/10.12952/journal.elementa.000071.

Sherrell, R.M., Annett, A.L., Fitzsimmons, J.N., Roccanova, V.J., Meredith, M.P., 2018. A "shallow bathtub ring" of local sedimentary iron input maintains the Palmer Deep biological hotspot on the West Antarctic Peninsula shelf. Philos. Trans. R. Soc. A Math. Phys. Eng. Sci. 376 https://doi.org/10.1098/rsta.2017.0171.

Shimmield, G.B., Price, N.B., 1986. The behaviour of molybdenum and manganese during early sediment diagenesis — offshore Baja California, Mexico. Mar. Chem. 19, 261–280. https://doi.org/10.1016/0304-4203(86)90027-7.

Sieber, M., Conway, T.M., de Souza, G.F., Hassler, C.S., Ellwood, M.J., Vance, D., 2021. Isotopic fingerprinting of biogeochemical processes and iron sources in the iron-limited surface Southern Ocean. Earth Planet. Sci. Lett. 567, 116967 https://doi.org/10.1016/j.epsl.2021.116967.

Smith, J.A., Graham, A.G.C., Post, A.L., Hillenbrand, C.D., Bart, P.J., Powell, R.D., 2019. The marine geological imprint of Antarctic ice shelves. Nat. Commun. 10 (1) https://doi.org/10.1038/s41467-019-13496-5.

St-Laurent, P., Yager, P.l., Sherrell, R.M., Stammerjohn, S.E., Dinniman, M.S., 2017. Pathways and supply of dissolved iron in the Amundsen Sea (Antarctica). J. Geophys. Res. Ocean. 122, 7135–7162. https://doi.org/10.1002/2017JC013162. Received.

St-Laurent, P., Yager, P.L., Sherrell, R.M., Oliver, H., Dinniman, M.S., Stammerjohn, S.E., 2019. Modeling the seasonal cycle of Iron and carbon fluxes in the Amundsen Sea Polynya, Antarctica. J. Geophys. Res. Ocean. 124, 1544–1565. https://doi.org/10.1029/2018JC014773.

Stockdale, A., Davison, W., Zhang, H., Hamilton-Taylor, J., 2010. The association of cobalt with iron and manganese (oxyhydr)oxides in marine sediment. Aquat. Geochem. 16, 575–585. https://doi.org/10.1007/s10498-010-9092-1.

Tagliabue, A., Bopp, L., Aumont, O., 2009. Evaluating the importance of atmospheric and sedimentary iron sources to southern ocean biogeochemistry. Geophys. Res. Lett. 36, 1–5. https://doi.org/10.1029/2009GL038914.

Vaillancourt, R.D., Balch, W.M., 2000. Size distribution of marine submicron particles determined by flow field-flow fractionation. Limnol. Oceanogr. 45, 485–492. https://doi.org/10.4319/lo.2000.45.2.0485.

van Manen, M., Aoki, S., Brussaard, C.P.D., Conway, T.M., Eich, C., Gerringa, L., Jung, J., Kim, T.-W., Lee, S.H., Lee, Y., Reichart, G.-J., Tian, H., Wille, F., Middag, R., 2022. The role of the Dotson Ice Shelf and circumpolar deep water as driver and source of dissolved and particulate iron and manganese in the Amundsen Sea polynya, southern ocean. Mar. Chem. 104161 https://doi.org/10.1016/j.marchem.2022.104161.

Vieira, L.H., Achterberg, E.P., Scholten, J., Beck, A.J., Liebetrau, V., Mills, M.M., Arrigo, K.R., 2018. Benthic fluxes of trace metals in the Chukchi Sea and their transport into the Arctic Ocean. Mar. Chem. 1–13 https://doi.org/10.1016/j.marchem.2018.11.001.

Vosteen, P., Spiegel, T., Gledhill, M., Frank, M., Zabel, M., Scholz, F., 2022. The fate of sedimentary reactive iron at the land-ocean interface: a case study from the Amazon Shelf. Geochem. Geophys. Geosyst. 23 (11).

Vraspir, J.M., Butler, A., 2009. Chemistry of marine ligands and siderophores. Annu. Rev. Mar. Sci. 1, 43–63.

Wåhlin, A.K., Graham, A.G.C., Hogan, K.A., Queste, B.Y., Boehme, L., Larter, R.D., Pettit, E.C., Wellner, J., Heywood, K.J., 2021. Pathways and modification of warm water flowing beneath Thwaites Ice Shelf, West Antarctica. Sci. Adv. 7, 1–10. https://doi.org/10.1126/SCIADV.ABD7254.

Wehrmann, L.M., Formolo, M.J., Owens, J.D., Raiswell, R., Ferdelman, T.G., Riedinger, N., Lyons, T.W., 2014. Iron and manganese speciation and cycling in glacially influenced high-latitude fjord sediments (West Spitsbergen, Svalbard): evidence for a benthic recycling-transport mechanism. Geochim. Cosmochim. Acta 141, 628–655. https://doi.org/10.1016/j.gca.2014.06.007.

Wells, M.L., Mayer, L.M., Guillard, R.R.L., 1991. A chemical method for estimating the availability of iron to phytoplankton in seawater. Mar. Chem. 33, 23–40. https://doi.org/10.1016/0304-4203(91)90055-2.

Wilch, T.I., McIntosh, W.C., Dunbar, N.W., 1999. Late Quaternary volcanic activity in Marie Byrd Land: potential 40Ar/39Ar-dated time horizons in West Antarctic ice and marine cores. GSA Bull. 111 (10), 1563–1580.

Witus, A.E., Branecky, C.M., Anderson, J.B., Szczuciński, W., Schroeder, D.M., Blankenship, D.D., et al., 2014. Meltwater intensive glacial retreat in polar environments and investigation of associated sediments: example from Pine Island Bay, West Antarctica. Quat. Sci. Rev. 85, 99–118.

Wolff-Boenisch, D., Gislason, S.R., Oelkers, E.H., Putnis, C.V., 2004. The dissolution rates of natural glasses as a function of their composition at pH 4 and 10.6, and temperatures from 25 to 74°C. Geochim. Cosmochim. Acta 68, 4843–4858. https://doi.org/10.1016/j.gca.2004.05.027.

Yoon, S.T., Lee, W.S., Nam, S.H., Lee, C.K., Yun, S., Heywood, K., et al., 2022. Ice front retreat reconfigures meltwater-driven gyres modulating ocean heat delivery to an Antarctic iceshelf. Nat. Commun. 13 (1), 1–8.